

Science and Technology of Nuclear Installations

# Interaction of Radiation with Matter and Related Topics

Guest Editors: Jakrapong Kaewkhao, Mitra Djamal, and Turgay Korkut





---

# **Interaction of Radiation with Matter and Related Topics**

Science and Technology of Nuclear Installations

---

## **Interaction of Radiation with Matter and Related Topics**

Guest Editors: Jakrapong Kaewkhao, Mitra Djamal,  
and Turgay Korkut



---

Copyright © 2014 Hindawi Publishing Corporation. All rights reserved.

This is a special issue published in “Science and Technology of Nuclear Installations.” All articles are open access articles distributed under the Creative Commons Attribution License, which permits unrestricted use, distribution, and reproduction in any medium, provided the original work is properly cited.

## Editorial Board

Nusret Aksan, Switzerland  
Antonio C. M. Alvim, Brazil  
Won Pil Baek, Republic of Korea  
Stephen M. Bajorek, USA  
George Bakos, Greece  
Jozsef Banati, Sweden  
Ricardo Barros, Brazil  
Anis Bousbia Salah, Belgium  
Giovanni B. Bruna, France  
Nikola avlina, Croatia  
Xu Cheng, China  
Leon Cizelj, Slovenia  
Alejandro Clausse, Argentina  
Francesco D' Auria, Italy  
Marcos P. de Abreu, Brazil  
Giovanni Dell'Orco, France  
Juan Carlos Ferreri, Argentina  
Nikolay Fil, Russia  
Cesare Frepoli, USA  
Giorgio Galassi, Italy  
Regina Galetti, Brazil

Michel Giot, Belgium  
Valerio Giusti, Italy  
Horst Glaeser, Germany  
Satish Kumar Gupta, India  
Ali Hainoun, Syria  
Keith E. Holbert, USA  
Kostadin Ivanov, USA  
Yacine Kadi, Republic of Korea  
Ahmed Khedr, Egypt  
Tomasz Kozlowski, USA  
Tomoaki Kunugi, Japan  
Mike Kuznetsov, Germany  
Hyeong-Y. Lee, Republic of Korea  
Bundit Limmeechokchai, Thailand  
Jiri Macek, Czech Republic  
Annalisa Manera, USA  
Borut Mavko, Slovenia  
Oleg Melikhov, Russia  
Rafael Mir, Spain  
Josef Misak, Czech Republic  
Rahim Nabbi, Germany

Manmohan Pandey, India  
Yuriy Parfenov, Russia  
Yves Pontillon, France  
Nik Popov, Canada  
Piero Ravetto, Italy  
Francesc Reventos, Spain  
Enrico Sartori, France  
Carlo Sborchia, France  
Massimo Sepielli, Italy  
Arkady Serikov, Germany  
James F. Stubbins, USA  
Iztok Tiselj, Slovenia  
Rizwan Uddin, USA  
Eugenijus Upuras, Lithuania  
Richard Wright, Norway  
Chao Xu, China  
X. George Xu, USA  
Yanko Yanev, Bulgaria  
Zhiwei Zhou, China  
Enrico Zio, Italy  
Massimo Zucchetti, Italy

## Contents

**Interaction of Radiation with Matter and Related Topics**, Jakrapong Kaewkhao, Mitra Djamal, and Turgay Korkut  
Volume 2014, Article ID 207484, 2 pages

**Neutron Radiation Tests about FeCr Slag and Natural Zeolite Loaded Brick Samples**, Vedat Veli Cay, Mucahit Sutcu, Osman Gencil, and Turgay Korkut  
Volume 2014, Article ID 971490, 5 pages

**Evaluation of the Detection Efficiency of LYSO Scintillator in the Fiber-Optic Radiation Sensor**, Chan Hee Park, Arim Lee, Rinah Kim, and Joo Hyun Moon  
Volume 2014, Article ID 248403, 6 pages

**Research of Dosimetry Parameters in Small Electron Beams**, Nazmiye Donmez Kesen, Aydin Cakir, Murat Okutan, and Hatice Bilge  
Volume 2014, Article ID 585219, 6 pages

**Detection Efficiency of NaI(Tl) Detector in 511–1332 keV Energy Range**, I. Akkurt, K. Gunoglu, and S. S. Arda  
Volume 2014, Article ID 186798, 5 pages

**Radiation Shielding Properties Comparison of Pb-Based Silicate, Borate, and Phosphate Glass Matrices**, Suwimon Ruengsri  
Volume 2014, Article ID 218041, 5 pages

**A Performance Evaluation of a Notebook PC under a High Dose-Rate Gamma Ray Irradiation Test**, Jai Wan Cho and Kyung Min Jeong  
Volume 2014, Article ID 362354, 8 pages

**The Application of Microdosimetric Principles to Radiation Hardness Testing**, Jeremy D. Northum and Stephen B. Guetersloh  
Volume 2014, Article ID 828921, 5 pages

## Editorial

# Interaction of Radiation with Matter and Related Topics

**Jakrapong Kaewkhao,<sup>1</sup> Mitra Djamal,<sup>2</sup> and Turgay Korkut<sup>3</sup>**

<sup>1</sup> Center of Excellence in Glass Technology and Materials Science (CEGM), Nakhon Pathom Rajabhat University, Nakhon Pathom 73000, Thailand

<sup>2</sup> Department of Physics, Faculty of Mathematics and Natural Sciences, Institute of Technology Bandung, Bandung 40132, Indonesia

<sup>3</sup> Department of Nuclear Energy Engineering, Faculty of Engineering, Sinop University, 57000 Sinop, Turkey

Correspondence should be addressed to Jakrapong Kaewkhao; [cegm.npru@gmail.com](mailto:cegm.npru@gmail.com)

Received 29 April 2014; Accepted 29 April 2014; Published 21 May 2014

Copyright © 2014 Jakrapong Kaewkhao et al. This is an open access article distributed under the Creative Commons Attribution License, which permits unrestricted use, distribution, and reproduction in any medium, provided the original work is properly cited.

In this volume we discuss the various types of radiation interaction with matter. The radiations of primary concern in this special volume originate in atomic or nucleus processes. They are conventionally categorized into six general types as follows:

- (i) charged particulate particle,
- (ii) fast electron,
- (iii) heavy charged particles,
- (iv) uncharged radiation,
- (v) electromagnetic radiation,
- (vi) neutron.

Fast electron includes beta particles (positive and negative) emitted in nuclear decay, as well as energetic electrons produced by any other process. Heavy charged particles denote a category that encompasses all energetic ions mass of one atomic unit or greater, such as alpha particles, proton, and fission products of many nuclear reactions. The electromagnetic radiation of interest includes X-rays emitted in rearrangement of electron shell of atom and gamma rays that originate from transitions within the nucleus itself. Neutrons generated in various nuclear processes constitute the final major category, which is often further divided into slow and fast neutron subcategories.

The scintillator research is addressed in two manuscripts. C. H. Park et al. were to develop and evaluate fiber-optic sensors. The fiber-optic radiation sensor using the  $(\text{Lu,Y})_2\text{SiO}_5:\text{Ce}$  (LYSO:Ce) scintillator was evaluated in terms of the detection efficiency and reproducibility for examining its applicability as a radiation sensor. I. Akkurt et al. measured the absolute efficiency; peak-to-valley ratio and energy resolution of a  $3'' \times 3''$  NaI(Tl) detector were determined experimentally for 511, 662, 835, 1173, 1275, and 1332 keV photon energies obtained from  $^{22}\text{Na}$ ,  $^{54}\text{Mn}$ ,  $^{60}\text{Co}$ , and  $^{137}\text{Cs}$  radioactive sources. This result is required for quality control of the experimental system.

Two of the manuscripts were studied for radiation shielding materials. Neutron shielding performances of new brick samples were developed by V. V. Cay et al. As a result, neutron shielding capacity of brick samples increases with increasing FeCr slag and natural zeolite percentages. This information could be useful in the area of neutron shielding. S. Ruengsri investigated the radiation shielding properties comparison of Pb-based silicate, borate, and phosphate glass matrices. The silicate and phosphate glass systems are more appropriate choices as lead-based radiation shielding glass than the borate glass system.

There are 3 manuscripts in applied radiation physics field in this volume. The application of microdosimetric principles to radiation hardness testing was proposed by J. D. Northum and S. B. Guetersloh, Texas A&M University. J. W. Cho and K. M. Jeong test a performance evaluation of a notebook PC under a high dose-rate gamma ray irradiation.

In their paper, N. D. Kesen et al. investigated dosimetry parameters in small electron beam.

By compiling these papers, we hope the scientists get important and new data for interaction of radiation with matter and related topics and the research should be continued.

*Jakrapong Kaewkhao  
Mitra Djamal  
Turgay Korkut*

## Research Article

# Neutron Radiation Tests about FeCr Slag and Natural Zeolite Loaded Brick Samples

Vedat Veli Cay,<sup>1</sup> Mucahit Sutcu,<sup>2</sup> Osman Gencel,<sup>3</sup> and Turgay Korkut<sup>4</sup>

<sup>1</sup> School of Aviation, Dicle University, 21280 Diyarbakir, Turkey

<sup>2</sup> Department of Materials Science and Engineering, Izmir Katip Celebi University, 35620 Izmir, Turkey

<sup>3</sup> Department of Civil Engineering, Faculty of Engineering, Bartin University, 74100 Bartin, Turkey

<sup>4</sup> Department of Nuclear Energy Engineering, Faculty of Engineering, Sinop University, Sinop, Turkey

Correspondence should be addressed to Osman Gencel; [osmangencel@gmail.com](mailto:osmangencel@gmail.com)

Received 20 November 2013; Accepted 2 March 2014; Published 10 April 2014

Academic Editor: Jakrapong Kaewkhao

Copyright © 2014 Vedat Veli Cay et al. This is an open access article distributed under the Creative Commons Attribution License, which permits unrestricted use, distribution, and reproduction in any medium, provided the original work is properly cited.

Neutron shielding performances of new brick samples are investigated. Brick samples including 10, 20, and 30 percentages of ferrochromium slag (FeCr waste) and natural zeolite are prepared and mechanical properties are obtained. Total macroscopic cross sections are calculated by using results of 4.5 MeV neutron transmission experiments. As a result, neutron shielding capacity of brick samples increases with increasing FeCr slag and natural zeolite percentages. This information could be useful in the area of neutron shielding.

## 1. Introduction

Bricks, made of different materials, are the most widely basic structures used in the world. The use of the brick dates back to 7500 BC. It has low cost. Also it is useful and widely produced as building material. There are too many studies about brick as construction and building material because of its widespread use. Also radiation shielding properties of bricks have been investigated in several papers. A radiation protection study was made about medical X-ray device. In this paper absorbed doses were obtained. Researchers have used tungsten-rubber sheets, lead, plasterboard, and bricks in shielding design [1]. In another study, a brick castle design was used to calibrate gamma radiation source [2]. Anthropogenic doses were studied on examples of some of the brick buildings suffered from radioactive contamination at 1949–1956 in Russia [3]. Responses of brick samples to gamma irradiation were investigated by Awadallah and Imran. As a result of this study, it is found that gamma ray attenuation coefficient of brick is higher than concrete [4]. Natural radioactivity levels of brick used for the construction of the dwelling in Iran area were determined [5]. Other materials

like water-extended polyester, to shield neutrons, have been studied [6], as well as concrete bricks with aggregates [7].

Despite these studies, studies about neutron shielding properties of brick are limited. Kharitonov developed a new technology for brick production and performed thermal neutron shielding experiments on produced sample. According to the results of this study, thermal neutron absorption capacity of brick is greater (about 75%) than graphite [8]. In other studies neutron radiography and neutron scattering techniques on brick samples were evaluated [9–12].

The number of applications including different radiation types increased rapidly in recent years. Therefore, radiation protection has become an important issue. There are several studies about usage of waste materials to design novel radiation protection materials [13–16].

Currently, since metallic ferrochrome production has increased, large quantities of their waste as ferrochromium slag occur at the result of the metallurgical processing. So, the recycling of wastes as ferrochrome slag is not only economically viable but also it is considered as an environmental friendly approach in the production of fired clay bricks. These bricks are low-cost building materials. These wastes may be

TABLE 1: Chemical composition of the raw materials used.

Compositions (wt.%)	Brick clay	Ferrochromium slag	Natural zeolite
Al <sub>2</sub> O <sub>3</sub>	15.7	23.47	11.82
SiO <sub>2</sub>	61.6	29.38	67.1
Fe <sub>2</sub> O <sub>3</sub>	6.8	1.55	1.47
MgO	2.3	38.5	1.15
CaO	2.16	0.93	2.16
K <sub>2</sub> O	2.36	0.06	3.43
Na <sub>2</sub> O	0.82	0.15	0.37
Cr <sub>2</sub> O <sub>3</sub>	—	5.17	—
LOI <sup>1</sup>	7.25	1.5	12.5

<sup>1</sup>Loss on ignition.

alternatively used in the brick body in order to produce a radiation protection material [8, 16, 17]. Mineralogical and compositional content of ferrochromium slag and zeolite is well matched with that of brick structure.

In present paper, FeCr slag and natural zeolite are added in brick commonly used in the construction of the buildings and neutron transmission experiments are performed. Seven different brick samples including different FeCr slag and natural zeolite percentages are irradiated 4.5 MeV neutron particles from <sup>241</sup>Am/Be fast neutron source. This study is important in terms of waste management and nuclear safety engineering areas.

## 2. Experimental Procedure

**2.1. Materials and Method.** In this study, production of radiation resistant bricks was accomplished from mixtures of brick clay and additives containing ferrochromium (FeCr) slag and natural zeolite. The physical and chemical properties of the raw materials were previously characterized. Chemical composition of the raw materials used is presented in Table 1. The raw materials were initially subjected to pre-treatments such as drying and ball milling. The raw materials subjected to ball milling sieved under 100 micron particle size. Chemical analysis of brick clay, FeCr slag, and zeolite was made by using X-ray fluorescence (XRF) spectrometer. Then, they were characterized by X-ray diffractometer (XRD) for their mineral content.

In this study, brick clay obtained from a brick manufacturer (Üç Yıldız Tuğla) in Bartın, Turkey, was used. Chemical analysis of the brick clay is presented in Table 1 in oxide form. According to the analysis, the clay includes a large fraction of SiO<sub>2</sub> in addition to Al<sub>2</sub>O<sub>3</sub>, Fe<sub>2</sub>O<sub>3</sub>, CaO, MgO, and K<sub>2</sub>O. Loss on ignition of brick raw material upon heating at 1000°C was measured as 7.25%. According to the XRD analysis, the clay includes mainly quartz, illite/muscovite (KAl<sub>2</sub>(AlSi<sub>3</sub>O<sub>10</sub>)(OH)<sub>2</sub>), and clinocllore ((Mg,Al,Fe)<sub>6</sub>(Si,Al)<sub>4</sub>O<sub>10</sub>(OH)<sub>8</sub>) constituents.

The ferrochromium slag is a waste material obtained from the manufacture of ferrochromium metal in the Eti Krom Works, Elazığ, Turkey. The specific gravity of slag is

TABLE 2: Prepared mixtures from the raw materials used (wt.%).

Mix code	Brick clay	Ferrochromium slag	Natural zeolite	Thickness (cm)
0	100	0	0	1.61
10F	90	10	0	1.94
20F	80	20	0	1.88
30F	70	30	0	1.90
10Z	90	0	10	1.77
20Z	80	0	20	1.87
30Z	70	0	30	2.03

3.17 g/cm<sup>3</sup>. The chemical composition of the slag used is presented in Table 1. The slag consists mainly of SiO<sub>2</sub>, Al<sub>2</sub>O<sub>3</sub>, and MgO in different phases such as spinel (MgO·Al<sub>2</sub>O<sub>3</sub>) and forsterite (MgO·SiO<sub>2</sub>) as well as chromium and iron oxides and fewer amounts of other metal oxides [16]. Another raw material is natural zeolite obtained from Rota Madencilik, Gördes, Turkey. The specific gravity of zeolite is 1.85 g/cm<sup>3</sup>. The chemical composition of the zeolite used is presented in Table 1. Natural zeolites have voids and three-dimensional systems of pore channels which are typically in the range of molecular dimensions. Zeolites are crystalline aluminosilicates containing elements such as sodium, potassium, magnesium, and calcium. X-ray analysis of the zeolite showed the characteristic peaks of clinoptilolite as well as presence of quartz, cristobalite, and K-feldspar.

**2.2. Brick Production Procedure.** Initially, the raw materials were dried at 100°C in a dry oven. Then, they were powdered by a ball mill. The mixtures containing brick clay with ferrochromium slag and natural zeolite addition prepared in a mixer. Brick clay was dispersed into water and was mixed with the selected additive (Table 2). Rectangular samples were formed by a slurry casting process. Prepared slurry mixtures were cast into the molds placed onto plaster blocks in order to suck excess water. In the meantime, top surface of the slurry was compressed by hand in order to ensure complete filling of the mold. Green samples were removed from the mold after 2 h and left to dry in ambient conditions for 24 h. Samples were further dried in an oven maintained at 50°C for 12 h and then at 100°C for 24 h. The dry samples were fired in a laboratory-type electrical furnace at the rate of 5°C/min until 900°C, for 2 hours.

Weight loss and dimensional changes of the samples were measured after drying and firing steps. Bulk density, apparent porosity and water absorption values of the fired samples were measured by Archimedes method. Their mechanical properties like compressive and bending strengths and also their microstructural analysis were performed.

The brick samples showed the dimensional stability during firing at 900°C and their linear shrinkages were almost zero. Table 3 shows the experimental results obtained from the brick samples fired at 900°C. One of produced brick sample is shown in Figure 1.

TABLE 3: Experimental results of the brick samples fired at 900°C.

Mix code	Weight loss (%)	Bulk density (g/cm <sup>3</sup> )	Porosity (%)	Water absorption (%)	Bending strength (MPa)	Compressive strength (MPa)
0	6.76	1.68	33.9	16.5	14.1	34.9
10F	5.88	1.83	34.6	16.1	13.5	32.0
20F	5.07	1.86	38.2	18.1	7.1	29.8
30F	4.69	1.90	38.6	17.4	9.2	27.5
10Z	7.54	1.65	37.4	20.3	8.2	22.3
20Z	8.17	1.56	39.3	22.4	6.5	19.4
30Z	8.36	1.48	42.8	25.9	6.1	14.3



FIGURE 1: Produced brick sample.

2.3. *Neutron Dose Transmission Experiments.* The alpha-beryllium isotopic neutron sources, like <sup>241</sup>Am/Be and <sup>239</sup>Pu/Be, and the spontaneous fission source like <sup>252</sup>Cf are widely used [18]. We used a <sup>241</sup>Am/Be alpha-beryllium neutron source to obtain primary neutron beam. Emitted radiations from this neutron source are shown in Table 4. In order to prevent the scattered neutrons, the source was placed in a box consisting of paraffin (against neutrons) and lead (against 59.54 keV <sup>241</sup>Am photons). As neutron detector, Canberra NP100B proportional neutron counter was used. Firstly, we measured without the sample between the source and detector. In this way background value ( $D_0$ ) was obtained. And then to determine  $D$  values for each sample, we measured with samples between the source and detector. To achieve 4.5 MeV neutron dose transmissions ( $T$ ),  $D$  values were divided by the value of  $D_0$  (see (1)):

$$T = \frac{D}{D_0}. \quad (1)$$

After dose transmission values were obtained, we applied (2) to calculate neutron total macroscopic cross sections,  $\Sigma$  for each samples [17–21]:

$$\Sigma = \frac{(\ln(1/T))}{x}. \quad (2)$$

In (2),  $x$  is thickness of sample.  $\Sigma$  value is an important parameter for neutron shielding issue. That is, macroscopic

TABLE 4: Radiation characteristics of <sup>241</sup>Am-Be neutron source<sup>1</sup>.

Principle Emissions	$E_{\max}$ (keV)	$E_{\text{eff}}$ (keV)	Specific activity: 127 GBq/g	
			Dose rate ( $\mu\text{Sv/h/GBq at 1 m}$ )	
Gamma/X-rays	13.9 (42.7%)	—	—	—
	59.5 (35.9%)			
	5.443 (12.8%)			
Alpha	5.486 (85.2%)	—	85	2
	—			
Neutron	—	4.5 MeV	2	—

<sup>1</sup>[http://stuarthunt.com/pdfs/Americium\\_241Beryllium.pdf](http://stuarthunt.com/pdfs/Americium_241Beryllium.pdf).

cross section value is directly proportional to the neutron shielding capacity of the sample. Experimental design for neutron transmission measurements is demonstrated in Figure 2.

### 3. Results and Discussion

The obtained results were evaluated for two different additives as natural zeolite and FeCr slag. Macroscopic cross-section value for the bare brick sample (without any additive) is about  $0.035 \text{ cm}^{-1}$ .

Macroscopic cross section results for natural zeolite additives (10, 20, and 30%) in mere brick sample with a polynomial fit can be seen in Figure 3. As can be seen in this figure, there is a peak value at 20% additive. In 20% point  $\Sigma$  is 0.09 and it is approximately three times greater than the sample without any additives. A decrease in macroscopic cross section after this value was detected. So, neutron shielding properties of brick can be increased by adding around 20 percent of zeolite.

Obtained  $\Sigma$  values for FeCr slag additives (10, 20 and 30%) with a linear fit were given in Figure 4. As shown in this figure, 4.5 MeV neutron macroscopic cross-section value increase with increasing FeCr slag additive. For example, at 30% point  $\Sigma$  is 0.102 and this value is three times greater than the bare brick sample. Linear fit shows that  $\Sigma$  is directly proportional to the adding FeCr slag percentage in bare brick.

The bulk density of brick sample without addition was  $1.68 \text{ g/cm}^3$ . The sample without addition had a porosity of

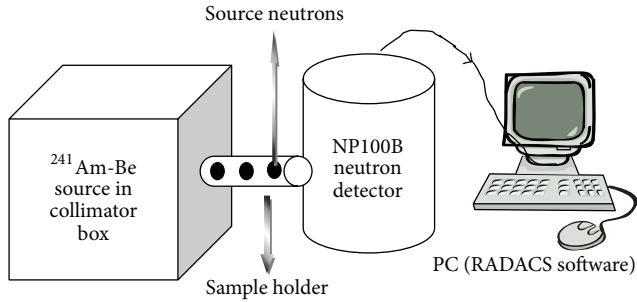


FIGURE 2: Experimental arrangement.

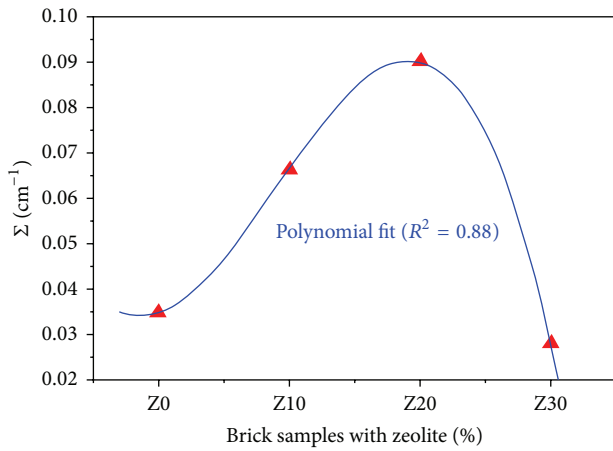


FIGURE 3: 4.5 MeV neutron macroscopic cross sections of bricks as a function of natural zeolite percentage.

33.9% and water absorption of 16.5%. The strengths of brick sample without addition were quite well.

The results of brick samples with ferrochromium slag obtained revealed that the bulk densities increased with an increase in the amount of the slag due to its high specific gravity. Bulk density of the bricks with the slag increased from 1.68 g/cm<sup>3</sup> to 1.90 g/cm<sup>3</sup>. In these samples, depending on the increase in the ferrochromium slag addition, porosity content and water absorption ratios of the samples increased; accordingly, their compressive strengths decreased.

The results of brick samples with natural zeolite obtained revealed that the bulk densities decreased with increasing of the zeolite content due to its porous structure. Bulk density of the bricks with the natural zeolite decreased from 1.68 g/cm<sup>3</sup> to 1.48 g/cm<sup>3</sup>. Depending on the increase in the zeolite addition, porosity and water absorption ratios of the samples increased, while the mechanical strengths were significantly reduced.

The bulk density of brick samples with combined additions showed a close value to that of the brick sample without addition. In these samples, depending on the increase in the ferrochromium slag and natural zeolite addition, porosity and water absorption ratios of the samples showed an increase; accordingly, their compressive strengths decreased. However, compressive and bending strengths of all samples

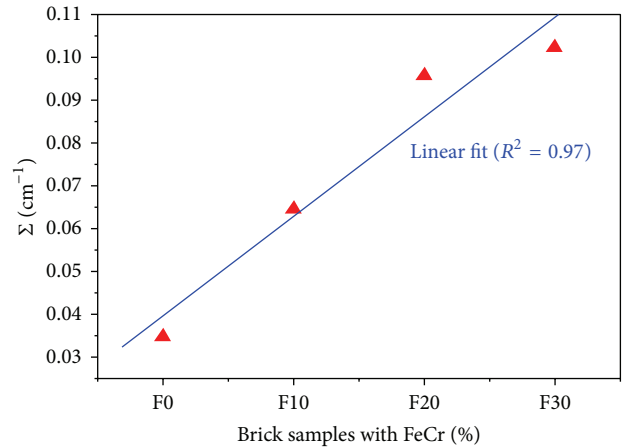


FIGURE 4: 4.5 MeV neutron macroscopic cross sections of bricks as a function of FeCr slag percentage.

were still higher than the Turkish and corresponding European Standards [19] for strength values.

#### 4. Conclusions

We prepared our samples using commercial bricks, FeCr slag, and natural zeolite with different percentages. While bulk density of bricks with FeCr slag increases, bulk density of bricks with zeolite decreases. Both bricks with FeCr slag and natural zeolite have sufficient strengths over 14 MPa. All bricks have high porosity that is desired to survive under elevated temperatures. Neutron absorption capability of brick increases with increasing FeCr slag and zeolite additives. The most important result of our study is to recover FeCr wastes in radiation shielding industries. Produced new samples may be used in constructions for protection against neutron radiation.

#### Conflict of Interests

The authors declare that there is no conflict of interests regarding the publication of this paper.

#### References

- [1] D. J. Eaton, R. Gonzalez, S. Duck, and M. Keshtgar, "Radiation protection for an intra-operative X-ray device," *British Journal of Radiology*, vol. 84, no. 1007, pp. 1034–1039, 2011.
- [2] E. R. van der Graaf, J. Limburg, R. L. Koomans, and M. Tijs, "Monte Carlo based calibration of scintillation detectors for laboratory and in situ gamma ray measurements," *Journal of Environmental Radioactivity*, vol. 102, no. 3, pp. 270–282, 2011.
- [3] M. O. Degteva, N. G. Bougrov, M. I. Vorobiova, P. Jacob, and H. Y. Göksu, "Evaluation of anthropogenic dose distribution amongst building walls at the Metlino area of the upper Techa River region," *Radiation and Environmental Biophysics*, vol. 47, no. 4, pp. 469–479, 2008.
- [4] M. I. Awadallah and M. M. A. Imran, "Experimental investigation of  $\gamma$ -ray attenuation in Jordanian building materials using

- HPGe-spectrometer,” *Journal of Environmental Radioactivity*, vol. 94, no. 3, pp. 129–136, 2007.
- [5] A. A. Fathivand, J. Amidi, and A. Najafi, “The natural radioactivity in the bricks used for the construction of the dwelling in Tehran areas of Iran,” *Radiation Protection Dosimetry*, vol. 123, no. 3, pp. 391–393, 2007.
- [6] H. R. Vega-Carrillo, E. Manzanares-Acuña, V. M. Hernández-Dávila, E. Gallego, A. Lorente, and I. Donaire, “Water-extended polyester neutron shield for a  $^{252}\text{Cf}$  neutron source,” *Radiation Protection Dosimetry*, vol. 126, no. 1–4, pp. 269–273, 2007.
- [7] E. Gallego, A. Lorente, and H. R. Vega-Carrillo, “Testing of a high-density concrete as neutron shielding material,” *Nuclear Technology*, vol. 168, no. 2, pp. 399–400, 2009.
- [8] V. I. Kharitonov, “Radiation shielding bricks from metallurgical products,” *Industrial Ceramics*, vol. 22, no. 3, pp. 169–174, 2002.
- [9] A. El Abd, A. Czachor, and J. Milczarek, “Neutron radiography determination of water diffusivity in fired clay brick,” *Applied Radiation and Isotopes*, vol. 67, no. 4, pp. 556–559, 2009.
- [10] M. N. Islam, M. K. Alam, M. A. Zaman, M. H. Ahsan, and N. I. Molla, “Application of neutron radiography to building industries,” *Indian Journal of Pure and Applied Physics*, vol. 38, no. 5, pp. 348–354, 2000.
- [11] G. C. Charalambopoulou, P. Karamertzanis, E. S. Kikkinides, A. K. Stubos, N. K. Kanellopoulos, and A. T. Papaioannou, “A study on structural and diffusion properties of porcine stratum corneum based on very small angle neutron scattering data,” *Pharmaceutical Research*, vol. 17, no. 9, pp. 1085–1091, 2000.
- [12] M. Erdem, O. Baykara, M. Dođru, and F. Kuluöztürk, “A novel shielding material prepared from solid waste containing lead for gamma ray,” *Radiation Physics and Chemistry*, vol. 79, no. 9, pp. 917–922, 2010.
- [13] A. El-Sayed Abdo, M. A. M. Ali, and M. R. Ismail, “Natural fibre high-density polyethylene and lead oxide composites for radiation shielding,” *Radiation Physics and Chemistry*, vol. 66, no. 3, pp. 185–195, 2003.
- [14] A. Rimpler, M. Börst, and D. Seifarth, “Neutron measurements around a TN85-type storage cask with high-active waste,” *Radiation Measurements*, vol. 45, no. 10, pp. 1290–1292, 2010.
- [15] M. Alwaeli and J. Nadziakiewicz, “Recycling of scale and steel chips waste as a partial replacement of sand in concrete,” *Construction and Building Materials*, vol. 28, no. 1, pp. 157–163, 2012.
- [16] O. Gencel, F. Koksall, C. Ozel, and W. Brostow, “Combined effects of fly ash and waste ferrochromium on properties of concrete,” *Construction and Building Materials*, vol. 29, pp. 633–640, 2012.
- [17] T. Korkut, O. Gencel, E. Kam, and W. Brostow, “X-ray, gamma and neutron radiation tests on epoxy-ferrochromium slag composites by experiments and Monte Carlo simulations,” *International Journal of Polymer Analysis and Characterization*, vol. 18, no. 3, pp. 224–231, 2013.
- [18] H. R. Vega-Carrillo, M. R. Martinez-Blanco, V. M. Hernandez-Davila, and J. M. Ortiz-Rodriguez, “Spectra and dose with ANN of  $^{252}\text{Cf}$ ,  $^{241}\text{Am}$ –Be, and  $^{239}\text{Pu}$ –Be,” *Journal of Radioanalytical and Nuclear Chemistry*, vol. 281, no. 3, pp. 615–618, 2009.
- [19] T. Korkut, A. Karabulut, G. Budak, B. Aygün, O. Gencel, and A. Hançerliođullari, “Investigation of neutron shielding properties depending on number of boron atoms for colemanite, ulexite and tincal ores by experiments and FLUKA Monte Carlo simulations,” *Applied Radiation and Isotopes*, vol. 70, no. 1, pp. 341–345, 2012.
- [20] T. Korkut, A. Ün, F. Demir et al., “Neutron dose transmission measurements for several new concrete samples including colemanite,” *Annals of Nuclear Energy*, vol. 37, no. 7, pp. 996–998, 2010.
- [21] T. Korkut, A. Karabulut, G. Budak, and H. Korkut, “Investigation of fast neutron shielding characteristics depending on boron percentages of  $\text{MgB}_2$ ,  $\text{NaBH}_4$  and  $\text{KBH}_4$ ,” *Journal of Radioanalytical and Nuclear Chemistry*, vol. 286, no. 1, pp. 61–65, 2010.

## Research Article

# Evaluation of the Detection Efficiency of LYSO Scintillator in the Fiber-Optic Radiation Sensor

Chan Hee Park, Arim Lee, Rinah Kim, and Joo Hyun Moon

*Dongguk University, Gyeongju Campus, 123 Dongdae-ro, Gyeongju, Republic of Korea*

Correspondence should be addressed to Joo Hyun Moon; [jhmoon86@dongguk.ac.kr](mailto:jhmoon86@dongguk.ac.kr)

Received 18 December 2013; Accepted 21 February 2014; Published 6 April 2014

Academic Editor: Jakrapong Kaewkhao

Copyright © 2014 Chan Hee Park et al. This is an open access article distributed under the Creative Commons Attribution License, which permits unrestricted use, distribution, and reproduction in any medium, provided the original work is properly cited.

The aim of this study was to develop and evaluate fiber-optic sensors for the remote detection of gamma rays in areas that are difficult to access, such as a spent fuel pool. The fiber-optic sensor consists of a light-generating probe, such as scintillators for radiation detection, plastic optical fibers, and light-measuring devices, such as PMT. The  $(\text{Lu},\text{Y})_2\text{SiO}_5:\text{Ce}$  (LYSO:Ce) scintillator was chosen as the light-generating probe. The  $(\text{Lu},\text{Y})_2\text{SiO}_5:\text{Ce}$  (LYSO:Ce) scintillator has higher scintillation efficiency than the others and transmits light well through an optical fiber because its refraction index is similar to the refractive index of the optical fiber. The fiber-optic radiation sensor using the  $(\text{Lu},\text{Y})_2\text{SiO}_5:\text{Ce}$  (LYSO:Ce) scintillator was evaluated in terms of the detection efficiency and reproducibility for examining its applicability as a radiation sensor.

## 1. Introduction

Workers should take extreme care when approaching high radiation areas, such as areas neighboring highly radioactive equipment or spent fuel pool, due to the risks of radiation exposure. To detect the radiation levels in those areas, it is necessary to develop a remote radiation detection system. The radiation levels surrounding the spent fuel pool are generally measured using the fixed type radiation detector system. Sometimes, the radiation levels on the water surface of the pool need to be measured using a portable radiation detector that a worker brings to the measurement point.

Optical fibers have been applied for remote radiation detection. Optical fibers have several advantages: intrinsic insensitivity to magnetic fields and electromagnetic interference, small size, and ability to perform distributed radiation measurements along a single fiber using optical time domain reflectometry techniques [1]. The applications of optical fiber technology include local dose deposition measurements and distributed hot-spots dose monitoring in nuclear waste storage facilities [2, 3]. The development of optical fiber radiation sensors has been driven mostly by medical applications such as in vivo real-time dosimetry [4]. The possibility of distributed optical fiber sensing technology was proven by

monitoring the large nuclear infrastructures, such as reactor containment buildings and radioactive waste repositories [5].

Optical fiber can be used not only as a radiation sensor but also as a medium for transmitting the light generated by a scintillator. In the field of X-ray and gamma ray medical imaging modalities, inorganic scintillators were selected as radiation in light converters [6–8]. The  $(\text{Lu},\text{Y})_2\text{SiO}_5:\text{Ce}$  (LYSO:Ce) scintillator was used for medical imaging [9]. This study adopted a  $(\text{Lu},\text{Y})_2\text{SiO}_5:\text{Ce}$  (LYSO:Ce) scintillator as the scintillator, which was connected to the optical fiber.

This paper developed and evaluated a radiation sensor using an optical fiber for the remote detection of gamma rays in real time in areas that are difficult to access, such as the spent fuel pool.

## 2. Method

*2.1. Material Selection and Characteristic Study of Optic Fibers and Scintillators.* The fiber-optic radiation sensor consisted of a radiation sensing probe, transmitting optical fiber, and data acquisition instruments. The fiber-optic radiation sensor should have a long transmitting optical fiber because it needs

TABLE 1: Main characteristics of inorganic scintillators [11].

Scintillator	BGO	YSO:Ce	LYSO:Ce	CsI:Tl	LSO:Ce
Effective Z number	83	35	<b>65</b>	51	66
Density (g/cm <sup>3</sup> )	7.13	4.45	<b>7.20</b>	4.51	7.40
Melting point (°C)	1,050	2,470	<b>2,100</b>	621	2,050
Refractive index	2.15	1.80	<b>1.82</b>	1.79	1.82
Light yield (%) * relative to NaI:Tl	15~20	80	<b>73~75</b>	50~100	~75
Peak wavelength (nm)	480	420	<b>420</b>	540	420
Decay time (ns)	300	70	<b>42</b>	1100	40

to detect the radiation level at a point far away from the radiation source.

This study chose a scintillator suitable for measuring gamma rays and evaluated its performance according to the optical fiber length. In general, the scintillator for gamma spectroscopy is the inorganic scintillator with a high atomic number. Table 1 shows that the light yield of the LYSO was approximately 4 times higher than the BGO. The scintillating materials with Ce-doped oxyorthosilicates are used in various fields. The Lu<sub>2</sub>SiO<sub>5</sub>:Ce(LSO:Ce) was widely known as very efficient, especially for medical imaging applications. It is due to high stopping power resulting from its high density, high light output, and fast response. The (Lu,Y)<sub>2</sub>SiO<sub>5</sub>:Ce(LYSO:Ce) shows similar properties. But the Lu<sub>2</sub>SiO<sub>5</sub>:Ce(LSO:Ce) is of high cost. (Lu,Y)<sub>2</sub>SiO<sub>5</sub>:Ce(LYSO:Ce) is a promising next generation scintillation crystal that is cheaper to produce [10]. Finally, the (Lu,Y)<sub>2</sub>SiO<sub>5</sub>:Ce(LYSO:Ce) was selected as the sensing probe of the fiber-optic sensor to detect gamma rays. This scintillator has an advantage for the remote detection of gamma rays because of its high density, high light output, fast decay time, good radiation hardness, high effective atomic numbers, nonhygroscopicity and stable physical and chemical properties, and ease of combining with the optical fiber. The (Lu,Y)<sub>2</sub>SiO<sub>5</sub>:Ce(LYSO:Ce) scintillator has a higher scintillation efficiency than the others and transmits light well through optical fibers because its refraction index is almost equal to the refractive index of the optical fiber. The (Lu,Y)<sub>2</sub>SiO<sub>5</sub>:Ce(LYSO:Ce) scintillator (Advanced Microwave Technologies Solution Co., Ltd) was 3 mm in diameter and 20 mm in length. The scintillator is cylinder type consistent with diameter of the optic fiber for easy to combine scintillator with optic fiber. To improve efficiency of light receiving, the surface of the scintillator is wrapped by Teflon reflective tape, attaching the holder to minimize the interference from ambient light. Table 1 lists the characteristics of the inorganic scintillators, including the (Lu,Y)<sub>2</sub>SiO<sub>5</sub>:Ce(LYSO:Ce).

The optical fiber normally used in the communication field is a glass optic fiber (GOF) made of quartz glass with high purity. The wide use of quartz glass optical fiber is due mainly to its outstanding optical properties, environmental safety, and thermal resistance. Although glass fibers have better thermal resistance than plastic fibers, glass fibers are fragile, difficult to be made into goods of any shape, and expensive. Therefore, the optic materials of high polymer

TABLE 2: Properties of the plastic optic fiber.

Plastic optic fiber (NY02, Edmund optics)	
Core	PMMA
Clad	Fluorine-PMMA
Numerical aperture	0.50
Operating temperature	-55°C~+70°C
Minimum radius of band	25 × outer diameter

TABLE 3: Properties of the photomultiplier.

Parameter	Description
Wavelength, nm	300–650
Peak wavelength, nm	420
Cathode	Bialkali
	22
Dynode	L
	10
Rise time, ns	1.5

have rapidly replaced glass optical fibers. Among them, plastic optic fibers (POFs) are the most widely used.

This study selected a plastic optic fiber (NY02, Edmund optics) with a diameter of 3 mm. NY02 consists of a core made of polymethylmethacrylate (PMMA) and a cladding made of fluorine polymethylmethacrylate (F-PMMA). Table 2 lists the properties of the plastic optic fibers chosen in this study.

**2.2. Experimental Setup.** The light-measuring device used in this study consisted of a radiation sensor probe, transmitting plastic optic fiber, photomultiplier tube (PMT), amplifier (AMP), and multichannel analyzer (MCA). The PMT used for the measurement was a H5211A (Hamamatsu), whose properties are summarized in Table 3. The PMT has response wavelengths of 300–650 nm as a head-on type. The main amplifier was the Canberra Amplifier model 2012. A power supply (C3830, Hamamatsu) was used to supply electric power to the PMT and preamplifier safely and simultaneously. The Ortec trump-8k-32+Maestro32 was used as the multichannel analyzer.

Figure 1 shows the experimental setup for a performance assessment of the remote fiber-optic radiation sensors. The fiber-optic radiation sensor was fabricated by attaching

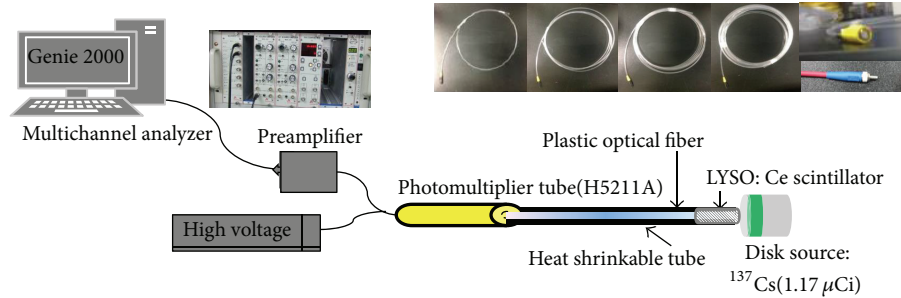


FIGURE 1: Experimental setup.

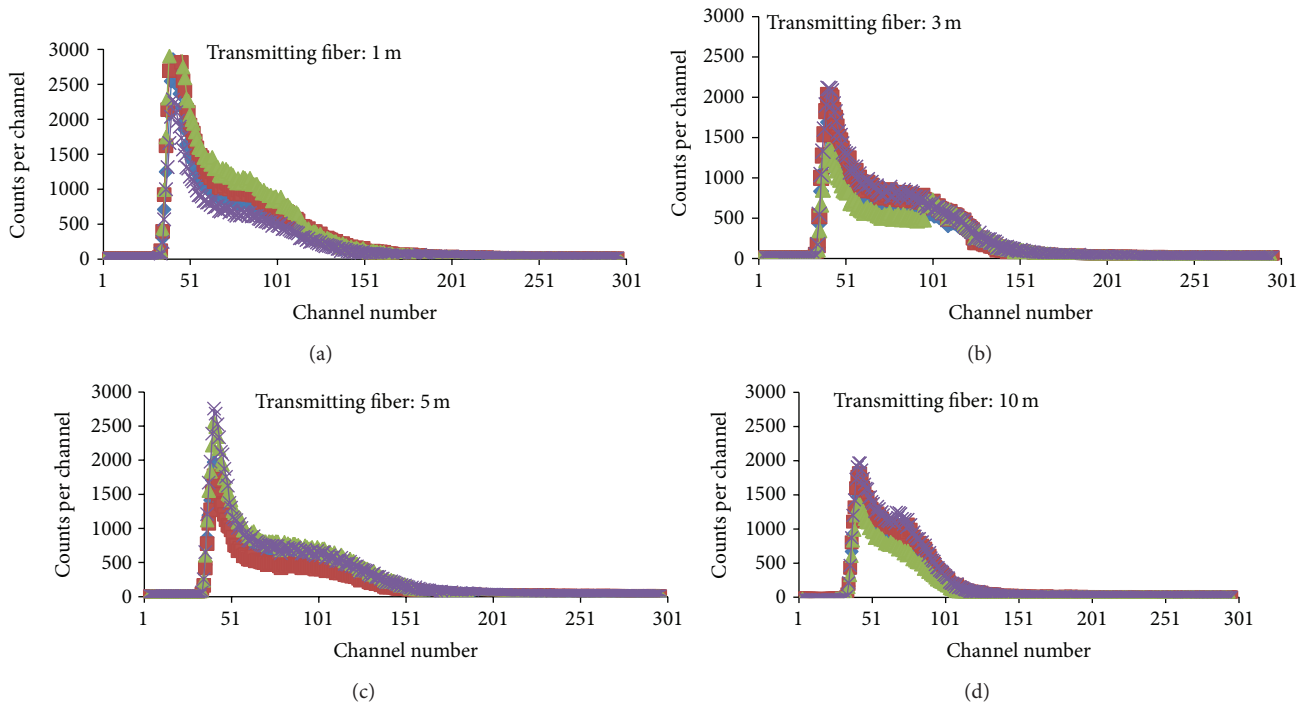


FIGURE 2: Reproducibility evaluation results of the fiber-optic radiation sensors according to the length of the transmitting optical fiber.

a scintillator to one-side end of the optical fiber using epoxy resin. To examine the effects of the length of the transmitting optical fiber, 4 types of the fiber-optic radiation sensors were fabricated: 1, 3, 5, and 10 m long. During the measurements, the bending angle of each fiber-optic radiation sensor was set to be the same so each optical fiber would have the same bending loss.

### 3. Results

Figure 2 shows the pulse height spectra of the fiber-optic radiation sensors against a Cs-137 source according to the length of the transmitting optical fiber. The reproducibility was evaluated 4 times according to the length of the optical fiber. Although the length changes, the overall shapes of the pulse height spectra were similar, except the case when the peak of the spectra when the length of the transmitting optical

fiber was 1 m was much higher than the other cases. On the other hand, the fiber-optic radiation sensor, 10 m in length, had the smallest standard deviation. The measurements showed that the 10 m long fiber-optic sensor can be used as a remote radiation sensor.

Figure 3 shows the pulse height spectra and total counts on average according to the length of the transmitting optical fiber. Similar to the reproducibility evaluation results, the comparison between the 1 m long transmitting optical fiber and others showed that the total counts by the 1 m long transmitting optical fiber were approximately 25–40% higher than the others.

Figure 4 shows the pulse height spectra according to the distance between the radiation sensor and the source, 0, 1, and 5 cm using the 1 m long transmitting optical fiber. The reproducibility was measured 4 times with the same distance between the radiation sensor and source. The shapes of the spectra of the 4 sensors were similar, but Figure 4 shows

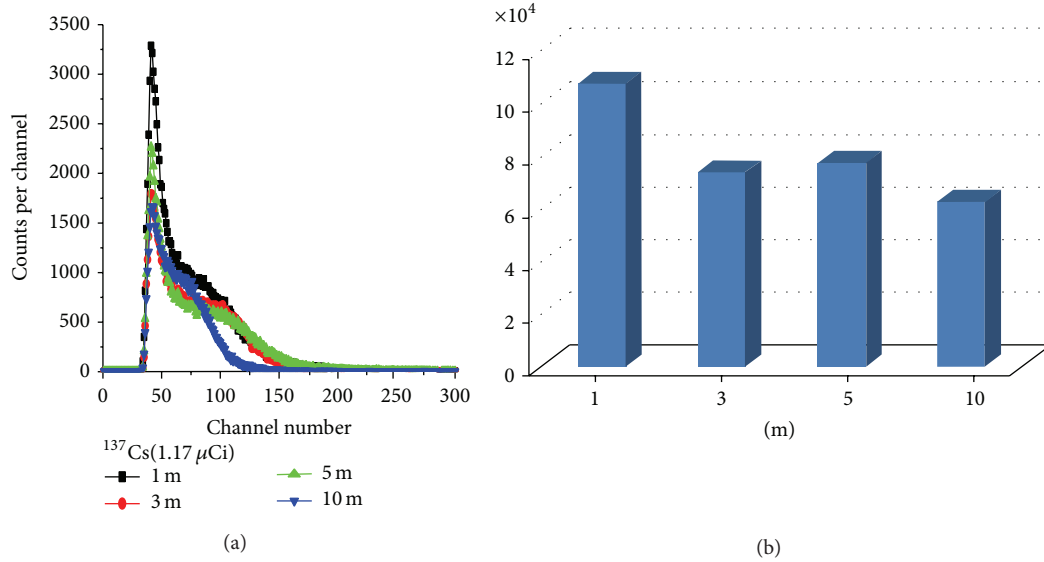


FIGURE 3: Pulse height spectra on the length of the transmitting optic fiber.

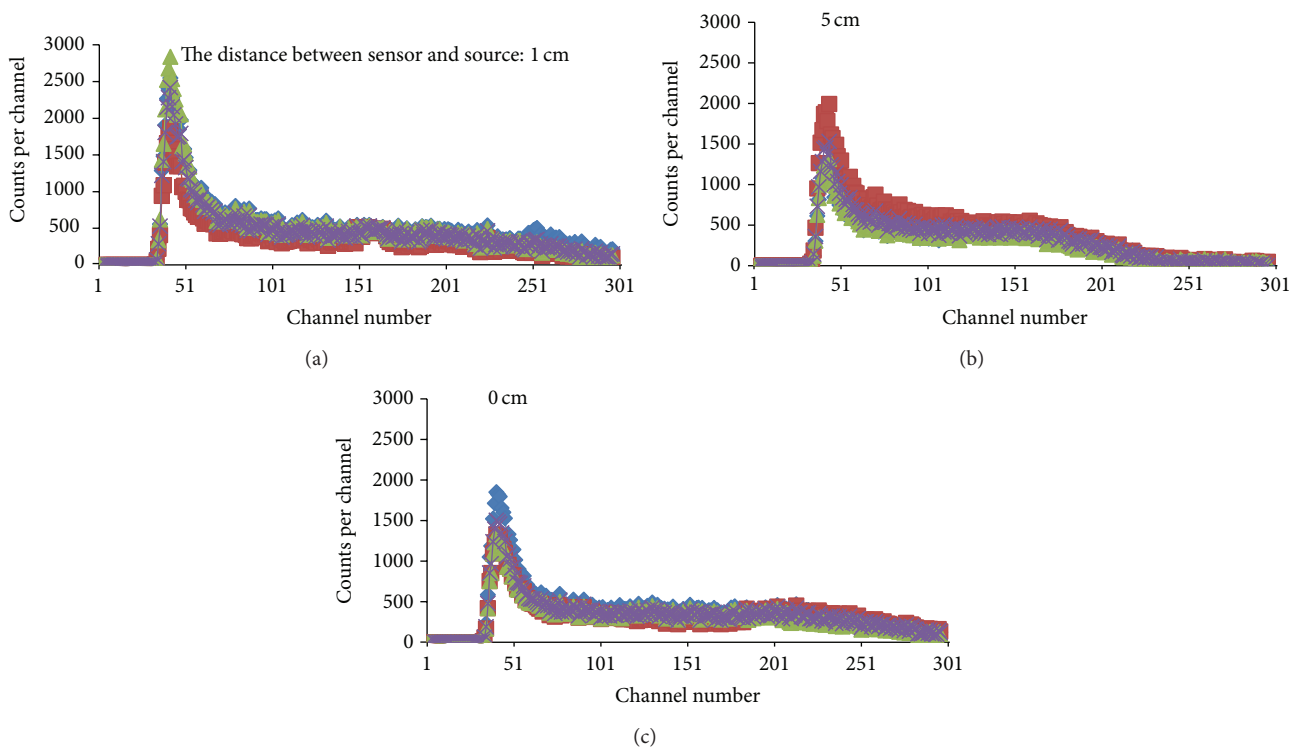


FIGURE 4: Reproducibility evaluation on the distance between the radiation sensor and the source.

that the efficiency of the case where the distance between the radiation sensor and source was 1 cm was higher than the other cases. On the other hand, the distance between the radiation and the source of 0 cm was found to have the smallest standard deviation.

Figure 5 shows the total counts according to (a) transmitting fiber length and (b) the distance between the fiber-optic sensor and source, respectively. As shown in Figure 5(a), the

detection efficiency of the transmitting fiber length of 1 m was the best, but the deviation in the total counts for the transmitting fiber length of 10 m was the lowest. The standard deviations in the total counts for 4 cases of the transmitting fiber length were 12 to 20%. In Figure 5(b), the detection efficiency for a distance of 1 cm between the fiber-optic sensor and radiation source was found to be the best. The standard deviations of the total counts for the 3 cases were less than 5%.

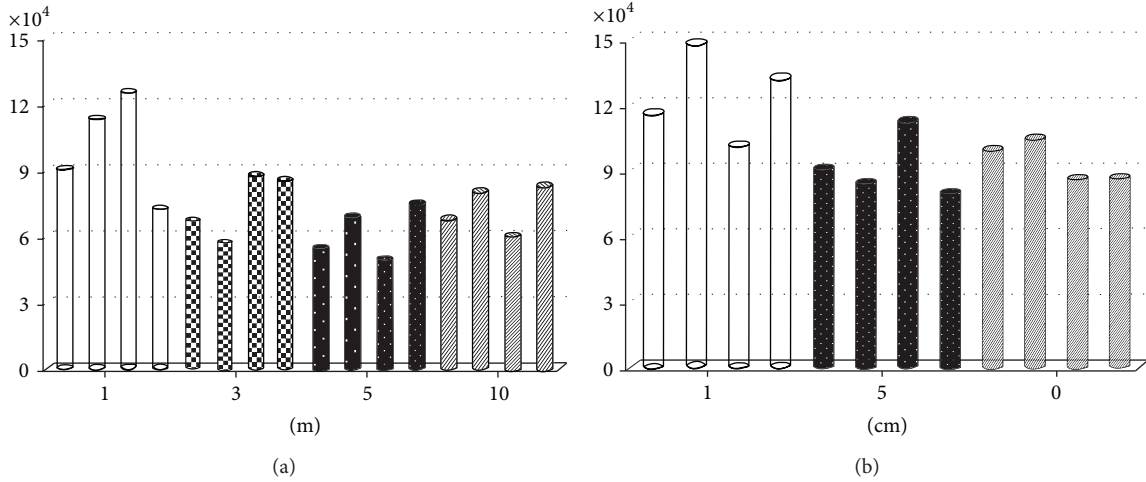


FIGURE 5: Total counts of the radiation sensor (a) according to the length of the transmitting optic fiber and (b) according to the distance between the radiation sensor and source.

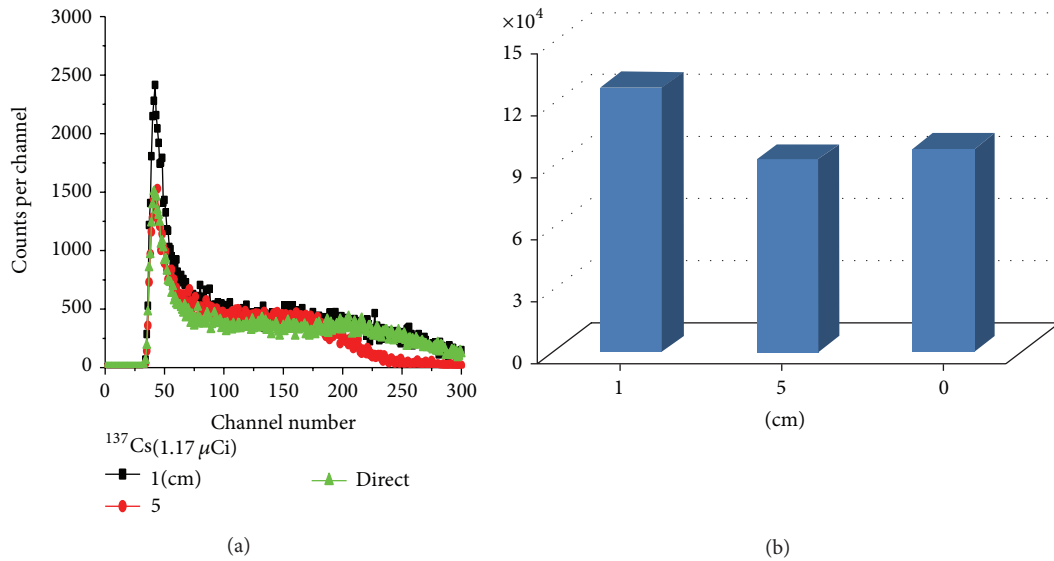


FIGURE 6: Pulse height spectra on the distance between the radiation sensor and source.

Figure 6 shows the pulse height spectra and means total counts as a function of the distance between the sensor and source. The comparison of the distance of 1 cm and the others showed that the pulse height at a distance of 1 cm was approximately 16–20% higher than the others. In this case, if the radiation sensor is located collinearly with the source, the signal detection efficiency decreased because the reaction area of the scintillator was relatively small.

The LYSO crystals have intrinsic radioactivity due to the Lu-176 isotope.  $^{176}\text{Lu}$  is a beta-emitter primarily decaying to an excited state of  $^{176}\text{Hf}$ . This isotope emits gamma photons with energies of 307 keV, 202 keV, and 88 keV [12]. The crystal's self-emission causes the crystal to be excited and produce scintillation light. This results in a self-count of 39 cps/g [13]. From this, it was evaluated that the intrinsic radioactivity included in the LYSO scintillator used in this study contributed to 8~10% of the total counts.

Reviewing all the measurements shows that the differences in the detection efficiencies of the fiber-optic sensors were due primarily to the geometrical arrangements of fiber-optic sensors and radiation source and polishing of the fiber-optic sensors and the connecting conditions between the scintillator and transmitting fiber. The polishing of LYSO scintillator and transmitting and the connection between them were manually performed. Hence, the connecting conditions could be a little different at each experiment.

#### 4. Conclusion

Using an inorganic scintillator and plastic optic fiber, the fiber-optic radiation sensor was developed and tested to examine the feasibility for remote detection of gamma rays in areas that are difficult to access, such as the spent fuel pool. The sensors were tested against a Cs-137 source, and

the test measurements were assessed according to the length of the transmitting optic fiber and the distance between the sensor and source. The measurements show that it is possible to measure the radioactive level remotely in a spent fuel pool, and so forth, using the optic fibers and an inorganic scintillator. This auxiliary radiation sensor is expected to have merit in cross-checking the main radiation level monitoring system simultaneously and minimizing the possibility of misjudging the situation in a spent fuel pool. The fiber-optic sensor was expected to enhance the stability and efficiency to minimize the radiation exposure of workers.

### Conflict of Interests

The authors declare that there is no conflict of interests regarding the publication of this paper.

### Acknowledgment

This study was supported by a National Research Foundation of Korea (NRF) grant funded by the Korean Government (MSIP) (Research Project no. NRF-2012M2A8A1027833).

### References

- [1] A. F. Fernandez, B. Brichard, S. O’Keeffe et al., “Real-time fibre optic radiation dosimeters for nuclear environment monitoring around thermonuclear reactors,” *Fusion Engineering and Design*, vol. 83, no. 1, pp. 50–59, 2008.
- [2] H. Bueker, F. W. Haesing, S. Nicolai, and B. Wolters, “Fiber-optic radiation dosimetry for medical applications,” in *Optical Fibers in Medicine V*, A. Katzir, Ed., vol. 1201 of *Proceedings of SPIE*, pp. 419–429, January 1990.
- [3] M. C. Decreton, V. Massaut, and P. Borgermans, “Potential benefit of fibre optics in nuclear applications: the case of the decommissioning and the waste storage activities,” in *Optical Fibre Sensing and Systems in Nuclear Environments*, vol. 2425 of *Proceedings of SPIE*, pp. 2–10, September 1994.
- [4] B. Brichard, A. F. Fernandez, H. Ooms, P. Borgermans, and F. Berghmans, “True dose rate enhancement effect in phosphorous doped fibre optic radiation sensors,” in *2nd European Workshop on Optical Fibre Sensors*, J. M. Lopez-Higuera and B. Culshaw, Eds., vol. 5502 of *Proceedings of SPIE*, pp. 184–187, esp, June 2004.
- [5] A. Fernandez Fernandez, P. Rodeghiero, B. Brichard et al., “Radiation-tolerant Raman Distributed Temperature monitoring system for large nuclear infrastructures,” *IEEE Transactions on Nuclear Science*, vol. 52, no. 6, pp. 2689–2694, 2005.
- [6] C. W. E. van Eijk, “Inorganic scintillators in medical imaging,” *Physics in Medicine and Biology*, vol. 47, no. 8, pp. R85–R106, 2002.
- [7] J. A. Mares, A. Beitlerova, M. Nikl et al., “Scintillation response of Ce-doped or intrinsic scintillating crystals in the range up to 1 MeV,” *Radiation Measurements*, vol. 38, no. 4–6, pp. 353–357, 2004.
- [8] V. V. Nagarkar, T. K. Gupta, S. R. Miller, Y. Klugerman, M. R. Squillante, and G. Entine, “Structured csi(tl) scintillators for x-ray imaging applications,” *IEEE Transactions on Nuclear Science*, vol. 45, no. 3, pp. 492–496, 1998.
- [9] S. Blahuta, A. Bessiere, D. Gourier, V. Ouspenski, and B. Viana, “Effect of the X-ray dose on the luminescence properties of Ce:Lyso and co-doped Ca, Ce:Lyso single crystals for scintillation applications,” *Optical Materials*, vol. 35, pp. 1865–1868, 2013.
- [10] I. Valais, C. Michail, S. David, C. D. Nomicos, G. S. Panayiotakis, and I. Kandarakis, “A comparative study of the luminescence properties of LYSO:Ce, LSO:Ce, GSO:Ce and BGO single crystal scintillators for use in medical X-ray imaging,” *Physica Medica*, vol. 24, no. 2, pp. 122–125, 2008.
- [11] <http://www.apace-science.com/>.
- [12] P. E. Valk, D. L. Bailey, D. W. Townsend, and M. N. Maisey, *Positron Emission Tomography: Basic Science and Clinical Practice*, Springer, 3rd edition, 2003.
- [13] J. Sæterstøl, *Characterization of Scintillation Crystals for Positron Emission Tomography*, University of Bergen, Bergen, Norway, 2010.

## Research Article

# Research of Dosimetry Parameters in Small Electron Beams

**Nazmiye Donmez Kesen, Aydin Cakir, Murat Okutan, and Hatice Bilge**

*Radiotherapy Department, Istanbul University Oncology Institute, Fatih, Capa, 34390 Istanbul, Turkey*

Correspondence should be addressed to Nazmiye Donmez Kesen; nazo94@gmail.com

Received 29 November 2013; Accepted 17 February 2014; Published 25 March 2014

Academic Editor: Jakrapong Kaewkhao

Copyright © 2014 Nazmiye Donmez Kesen et al. This is an open access article distributed under the Creative Commons Attribution License, which permits unrestricted use, distribution, and reproduction in any medium, provided the original work is properly cited.

In this study, dose distributions and outputs of circular fields with dimensions of 5 cm and smaller, for 6 and 9 MeV nominal energies from the Siemens ONCOR Linac, were measured and compared with data from a treatment planning system using the pencil beam algorithm in electron beam calculations. All dose distribution measurements were performed using the GafChromic EBT film; these measurements were compared with data that were obtained from the Computerized Medical Systems (CMS) XiO treatment planning system (TPS). Output measurements were performed using GafChromic EBT film, an Advanced Markus ion chamber, and thermoluminescent dosimetry (TLD). Although it is used in many clinics, there is not a substantial amount of detailed information in the literature about use of the pencil beam algorithm to model electron beams. Output factors were consistent; differences from the values obtained from the TPS were at maximum. When the dose distributions from the TPS were compared with the measurements from the ion chamber and GafChromic EBT films, it was observed that the results were consistent with 2 cm diameter fields and larger, but the outputs for 1 cm diameter fields and smaller were not consistent.

## 1. Introduction

In recent years, electron beams, rather than low X-ray beams, have been used for the treatment of superficial lesions, because of the different dosage characteristics of the two sources. Tumours which are close to critical body structures require small directionality error margins and thus require small treatment fields. Electron beams have uniform dose distribution at the surface and a rapid decrease in the dose below a specific depth [1].

Electron beam therapy is an indispensable practice in radiotherapy, and therefore most commercial treatment planning systems use electron beam programs alongside photon planning programs. Electron beam dose calculations were originally based on empirical functions that utilised ray line geometries [2, 3]. More advanced pencil beam algorithms are based on multiple scattering theories [4, 5]. The major limitation of both empirical methods and pencil beam algorithms is their inability to predict depth dose distributions and accurately monitor units for small field sizes. A Monte Carlo-based dose calculation algorithm has been investigated by several groups. The accuracy of implementation of this algorithm was found to be more reliable than that of other algorithms. A commercial Monte

Carlo-based dose calculation algorithm has become available for electron beam treatment planning systems. Nevertheless, pencil beam algorithms are still used for electron beam treatment planning in many oncology clinics.

There are several theoretical and experimental methods described in the literature for determination of the dose distribution and prediction of the electron beam output factors. Film dosimetry is the most rapid method to obtain the dose distribution and related output factors.

Dose distributions for small circular electron beams from the Siemens Oncor linear accelerator using GafChromic EBT films were measured. Output factors were measured using GafChromic EBT films, TLD, and the Advanced Markus ion chamber. The measured values were compared with CMS XiO treatment planning system data, which uses the pencil beam algorithm.

## 2. Methods and Materials

**2.1. Isodose Distribution Measurements.** The source of electron beams used for this study was a high energy linear accelerator (Siemens Oncor, Germany). The linear accelerator had a circular cone with diameter 5 cm that was used as

the standard cone. Cut-outs were prepared to achieve fields with diameters of 1, 2, 3, and 4 cm.

Dose distribution measurements were made for these circular fields, 1–5 cm in diameter, using a MP3-M automatic water phantom and a Semiflex (0.125 cc) ion chamber (PTW-New York Corp., Hicksville, NY), with a source-to-surface distance (SSD) of 100 cm. 1, 2, 3, and 4 cm cut-outs were placed into the 5 cm diameter standard circular cone. For profile measurements range reference ( $R_{ref}$ ), dose range of 85% ( $R_{85}$ ), dose range of  $(85\%)/2$  ( $R_{85/2}$ ), dose range of 50% ( $R_{50}$ ), and practical range ( $R_p$ ) depth values were used for all electron energies and were obtained from percentage depth dose curves measured using a  $10 \times 10 \text{ cm}^2$  standard cone. Depth dose measurements were repeated for all small fields. Profiles and depth dose curves were put into the PTW Verisoft software program (PTW-New York Corp., Hicksville, NY) and isodose curves were obtained.

In film dosimetry, GafChromic EBT films (International Specialty Products, Wayne, NJ, USA) were used because of their characteristic null energy response. GafChromic EBT films are more sensitive than older radiochromic films and are readily available for photon dosimetry as well as electron dosimetry [6]. The measurable dose range is 1–800 cGy. EBT films have a relatively small effective thickness; as such the effective measurement point was neglected. For calibration of films, a 9 MeV electron beam was used; each film was oriented perpendicular to the central axis of the electron beam, at the centre of the beam, in a solid water phantom. Films were placed at the depth of maximum dose (20 mm). The calibration curve was obtained by exposing films in a  $10 \times 10 \text{ cm}^2$  field, with doses ranging from 10 to 800 cGy. All exposed films were considered after 24 h, because the darkening saturation of films must be allowed to occur [7].

Films were scanned using a flatbed colour scanner (EPSON America Inc., Long Beach, CA), collected using its software program, and analyzed using the ImageJ program; films were separated into three colours: red, blue, and green. For optimum contrast, the red image was selected for film dosimetry, because the peak absorption of the EBT film is in the red region of the visible spectrum. Besides measuring the characteristics of all exposed films, a nonexposed film was scanned to measure the background effect. All films were placed inside the scanner in the same direction, because of the orientation problem. Permeability at the centre of the exposed films was observed using the Mephysto mcc software program (PTW-New York Corp., Hicksville, NY) and a calibration curve was generated.

To obtain the isodose distributions, films were oriented parallel to the electron beam in a solid water phantom. The setup is shown in Figure 1. Alongside the 5 cm standard circular cone, the 1–4 cm diameter cut-outs were used, and films were exposed with 6 and 9 MeV nominal energies. Isodose curves were generated using the calibration curve in the PTW Verisoft program.

The XiO therapy planning system (TPS) (CMS-Elekta AB, Stockholm), with its pencil beam algorithm, was used for calculation of the isodose curves. XiO TPS does not support circular cones; the system only has square field electron beam

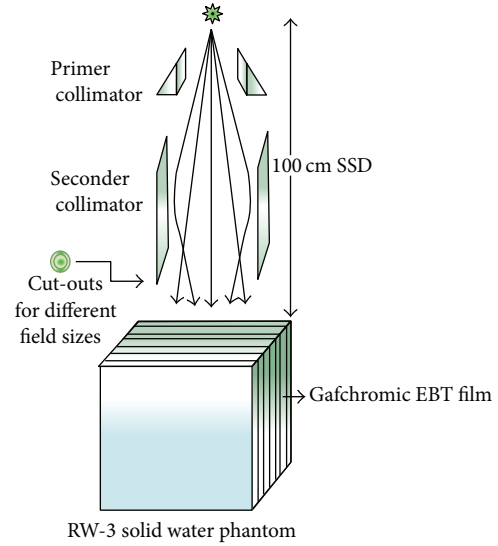


FIGURE 1: Solid water phantom setup used for isodose distribution measurements. GafChromic films were aligned parallel to the electron beam in solid water phantom.

data. Therefore, the smallest cone,  $10 \times 10 \text{ cm}^2$ , was blocked to obtain 5, 4, 3, 2, and 1 cm field sizes in the planning system. Isodose distributions were calculated using the pencil beam algorithm and fluence maps of isodoses were obtained for all energies using a solid phantom. Fluence maps were transferred into the PTW Verisoft program and converted into isodose curves.

To provide comparisons of multidimensional dose distributions, dose comparison tools such as gamma dose distribution, distance-to-agreement (DTA), and dose difference (DD) have been developed [8, 9]. The gamma dose distribution tool was used in our study. A DD of 3% and 3 mm DTA gamma evaluation parameters were used for analysis. Sagittal isodose distributions along the central axis were measured using EBT film and were compared with data that were calculated using the treatment planning system.

**2.2. Output Factor Measurements.** Output factor measurements were performed for 6 and 9 MeV electron beams in a  $40 \times 40 \text{ cm}^2$  solid water phantom at 100 cm SSD, using the PTW Unidos (Freiburg, Germany) electrometer, Advanced Markus ion chamber, films, and TLD. Reference depths were determined for each electron energy from the IAEA 398 protocol, using the formula below: [10]

$$D_{ref} = 0.6R_{50} - 0.1 \text{ g/cm}^2 \quad (R_{50}, \text{g/cm}^2), \quad (1)$$

where  $R_{50}$  (cm or  $\text{g/cm}^2$ ) is the depth of the beam when the dose is equal to 50% of the maximum dose.

The  $D_{ref}$  values for 6 and 9 MeV electron beams were 1.3 and 2 cm, respectively. Outputs were measured for 5, 4, 3, 2, and 1 cm circular fields using the cerrobend cut-outs within a 5 cm circular cone. Output factors were obtained and normalised to the  $10 \times 10 \text{ cm}^2$  field.

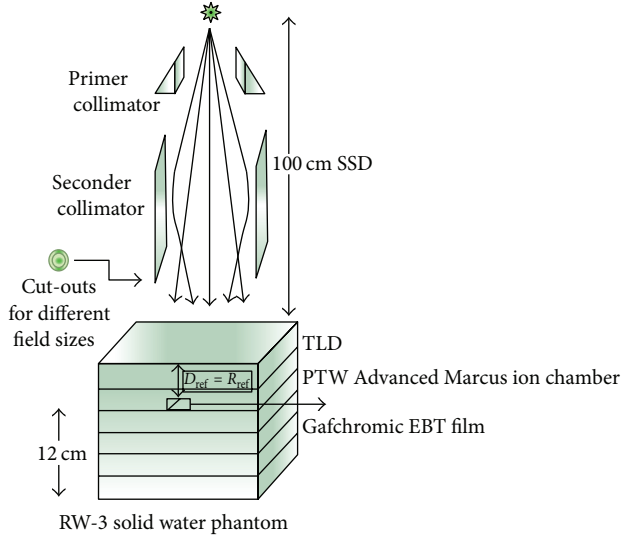


FIGURE 2: Output factor measurements were obtained with solid water phantoms which were aligned perpendicular to the electron beam.

Output factors were measured using the Advanced Markus ion chamber (PTW-New York Corp., Hicksville, NY), GafChromic EBT film, and TLD. Phantoms were positioned perpendicular to the beam direction. 100 MU was defined for both the ion chamber and TLD measurements. The experimental setup is shown in Figure 2.

GafChromic EBT film was oriented perpendicular to the direction of the incident electron beam, and care was taken to align the beam to the centre of the film. For all field sizes, 400 MU was considered to provide sufficient darkness on the films. All films were scanned the following day and separated into colour scales; the red measurement was selected and recorded. Point permeability, which was measured at the field centre, was converted into a dose (Gy). All films used were from the same batch and irradiated on the same day.

For TLD measurements,  $1 \times 1 \times 1 \text{ mm}^3$  TLD rods and a GR-200R1 Fimel reader were used. Ternary groups were not used because of the small measurement size considered. One TLD was positioned on the custom-built phantom and irradiated with 100 MU at the reference depth. Irradiation was repeated five times and the average of the readings was taken. TLD rods were read with the Fimel-LTM; output factors were obtained and normalised to a  $10 \times 10 \text{ cm}^2$  field size.

In the CMS TPS, a  $10 \times 10 \text{ cm}^2$  standard cone was blocked to generate 5, 4, 3, 2, and 1 cm diameter circular fields. For 6 and 9 MeV electron beams, the MU calculation was carried out in the TPS, considering 100 cGy at the reference depth along the central axis. Output factors were determined from the MU values. Output factors obtained from the TPS were compared with the factors that were found using other dosimetric methods.

### 3. Results and Discussion

For 6 and 9 MeV electron beams, 100% ( $d_{\text{max}}$ ), 90%, 80%, 50%,  $R_p$ ,  $E_{p0}$ , and  $E_0$  values were obtained from the depth

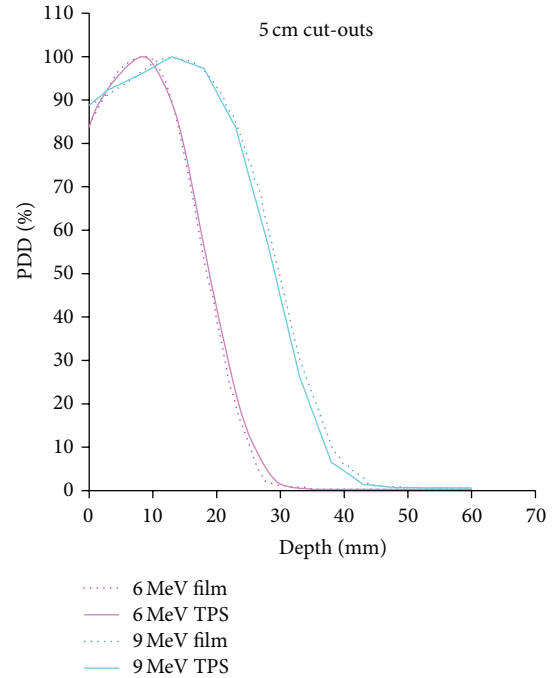


FIGURE 3: Percent depth dose curve comparisons between measured data using Semiflex ion chamber and EBT films using 5 cm circular cone at 100 cm SSD. All curves are normalized to 100%. As measurements made by Semiflex ion chamber are represented by solid lines, EBT film measurements are represented by dotted lines.

dose measurements. These were carried out using a Semiflex ion chamber with a volume of 0.125 cc, and the  $10 \times 10 \text{ cm}^2$  field values are shown in Table 1.

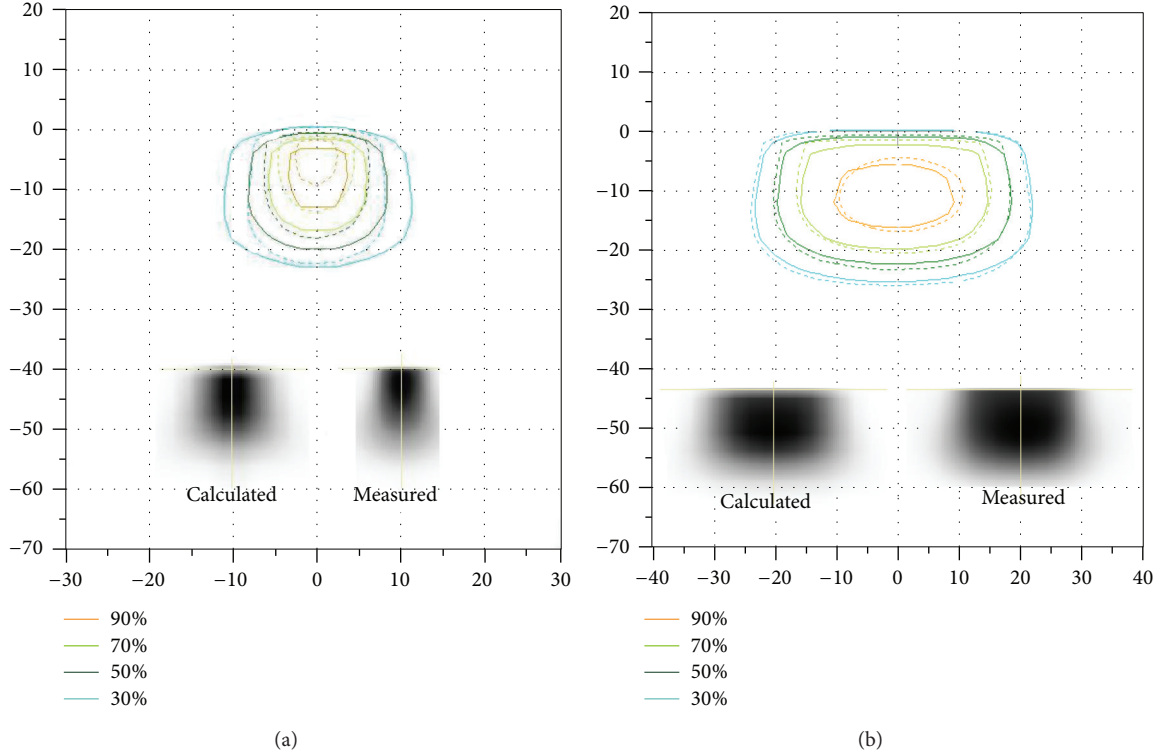
For the 6 MeV electron beam, the  $d_{\text{max}}$  value obtained from the Semiflex ion chamber (0.125 cc) is 12 mm in the  $10 \times 10 \text{ cm}^2$  square field size. The depth dose characteristics of electrons change dramatically with decreasing field sizes. For all electron energies, the maximum depth decreases with decreasing field sizes. In other words, when the field size was reduced, the maximum dose point moved closer to the surface. The most probable reason for this is the chamber volume effect. For chambers, therapeutic ranges decrease with field size, and the falloff region of the curve becomes less steep. This is consistent with Sharma et al.'s observations [11]. In addition, with decreasing field size, a decreasing degree of lateral electronic equilibrium will be present at the central axis, and the depth dose and output factors will show large sensitivity to the field shape and size [1].

Figure 3 shows a comparison of the measured data that were obtained from the Semiflex ion chamber and EBT films for a 5 cm circular cone at 100 cm SSD. The agreement between calculated and measured data is good.

The depth dose measurements obtained from the Semiflex ion chamber and film were converted to isodoses using the PTW Verisoft program. These isodoses were compared with isodoses generated from TPS. Comparisons were carried out using the gamma index method. For this method, the tolerance limit selected was 3 mm DTA, 3% DD. When the dose distributions from the TPS were compared with

TABLE 1: 100% ( $d_{\max}$ ), 90%, 80%, 50%,  $R_p$ ,  $E_{p0}$ , and  $E_0$  values obtained from the depth dose measurements for 6 and 9 MeV electron beams.

	$10 \times 10 \text{ cm}^2$	$R_{100}$ (mm)	$R_{90}$ (mm)	$R_{80}$ (mm)	$R_{50}$ (mm)	$R_p$ (mm)	$E_{p0}$ (mm)	$E_0$ (mm)
6 MeV	Semiflex ion chamber	12	16.77	18.59	22.68	28.80	5.94	5.29
9 MeV	Semiflex ion chamber	19.50	27.66	30.54	36.41	45.52	9.28	8.55

FIGURE 4: Sagittal isodose comparisons of a 6 MeV beam along the central axis for 1 (a) cm and 4 (b) cm circular cutouts using a 5 cm diameter circular cone. Solid lines represent calculations and dotted lines represent measurements ( $x$ -axis and  $y$ -axis are in cm).

those from the Semiflex ion chamber and EBT films, it was seen that the results were consistent with field sizes of 2 cm diameter and larger. For 1 cm diameter fields, isodoses were incompatible at the central axis for 6 and 9 MeV electron beams. With increasing energy and decreasing field size, the isodoses of the individual methods are no longer consistent with each other.

Figures 4 and 5 show, as an example, a sagittal isodose comparison between calculated and measured data for 6 and 9 MeV beams, at 100 cm SSD using 4 cm and 1 cm cut-out sizes.

Outputs obtained using different measurement methods for 6 and 9 MeV nominal energies, for field sizes of 5, 4, 3, 2, and 1 cm diameter, are shown in Table 2. All measurements were made with a cone distance of 95 cm.

TLD results have average values for all fields between the values obtained for ion chamber and film measurements. However, generally, with increasing energy level and field size, output factor differences decrease.

For all energies and field sizes, output factors were consistent; differences were found to be, at maximum, 27%, compared with the values from the TPS.

In the literature, there is no evidence of studies concerning electron beam outputs for field sizes smaller than  $5 \times 5 \text{ cm}^2$  using the pencil beam algorithm. In recent years, it has been discovered that the Monte Carlo algorithm gives more accurate results than the pencil beam algorithm.

The results of comparisons using gamma analysis (3% and 3 mm) are shown in Figure 6. The agreement between measured and calculated dose distribution values was very good for both 4 and 3 cm cut-outs. For the 2 cm cut-out, agreement was good at the centre of the field but poor at the edge. Agreement was very poor for the 1 cm cut-out at both 6 and 9 MeV.

It was observed that results obtained at 6 MeV were consistent, and consistency was good at both the high and low dose regions at this energy. However, with increasing energy, this consistency reduced. With increasing energy, comparable results were obtained in the low dose region but not in the high dose region. This is due to the high dose falling region; the accuracy of the gamma index comparison decreases.

A comparison was made between the calculated and measured depth doses, isodose distributions, and outputs for 6 and 9 MeV and 4, 3, 2, and 1 cm circular cut-outs using

TABLE 2: Percentage differences between calculated and measured outputs from different measurement methods at 6 and 9 MeV nominal energies for 5, 4, 3, 2, and 1 cm field sizes. For both energies,  $10 \times 10 \text{ cm}^2$  field size was assumed for TPS values.

	5 cm	4 cm	3 cm	2 cm	1 cm
6 MeV					
Advanced Markus-TPS	21%	24%	27%	21%	17%
EBT film-TPS	18%	20%	21%	15%	3%
TLD-TPS	20%	22%	27%	15%	9%
9 MeV					
Advanced Markus-TPS	10%	14%	19%	17%	16%
EBT film-TPS	7%	10%	13%	13%	7%
TLD-TPS	8%	10%	15%	12%	5%

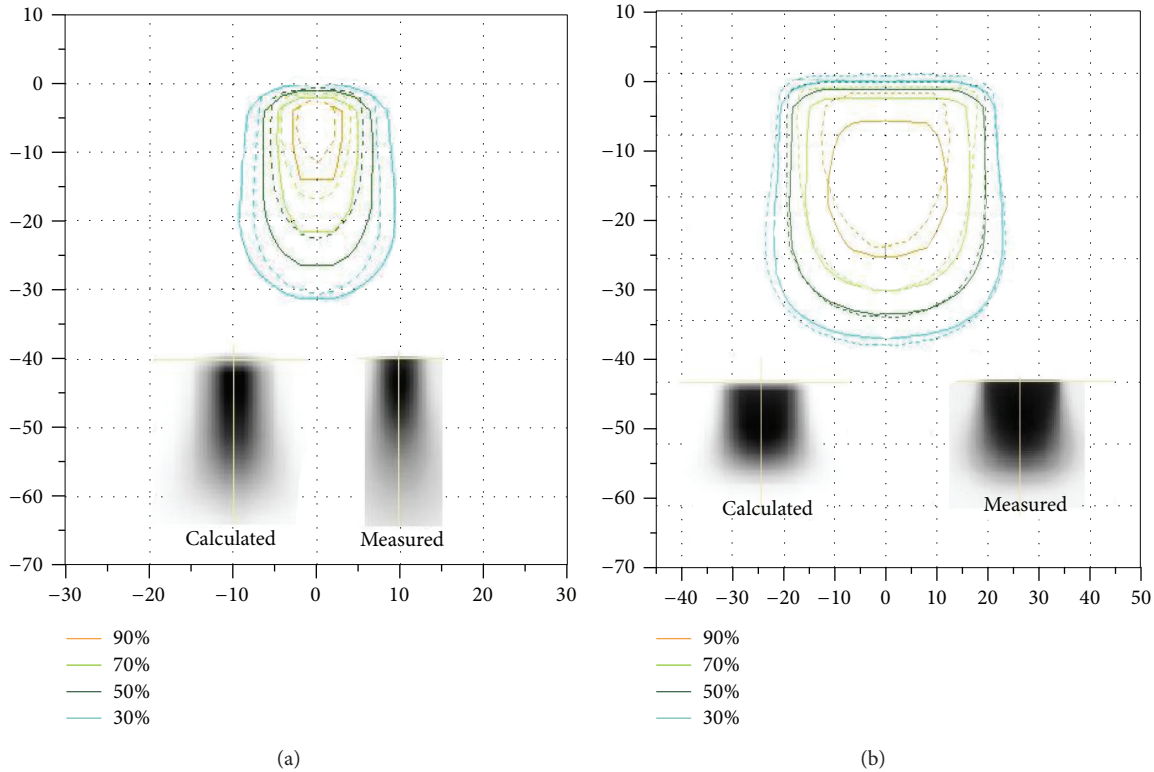


FIGURE 5: Sagittal isodose comparisons of a 9 MeV beam along the central axis for 1 (a) cm and 4 (b) cm circular cut-outs using a 5 cm diameter circular cone. Solid lines represent calculations and dotted lines represent measurements ( $x$ -axis and  $y$ -axis are in cm).

a 5 cm standard circular cone. Our study shows that pencil beam algorithm can be used to accurately predict depth doses and isodose distributions for fields with diameter as small as 3 cm at 100 cm SSD. When the cutout size is smaller than 3 cm, the circular calculated dose distribution can differ significantly from the measurement at 100 cm SSD. MUs obtained from the planning system were different from the measurements for all circular cutouts using the 5 cm circular cone. This is consistent with results reported by Xu et al. [12]. The most important limitation of the pencil beam algorithm is its failure to predict depth dose distributions and accurate MUs for field sizes smaller than the extent of the lateral scatter equilibrium [12]. It has also been observed in our study that pencil beam algorithm should not be used for MU calculations for small electron field sizes.

The American Association of Physics in Medicine (AAPM) recommends that because of their high spatial

resolution, films should be primarily chosen for electron beam dosimetry. This is supported by the fact that the film dose-response curve was found to be weakly dependent on the electron beam energy (within  $\pm 4\%$ ) [13]. In addition, in our output factor measurements, it was seen that GafChromic EBT film measurement results were closer to the calculated results than other dosimetric methods. In the literature, it is suggested that before using detectors for determination of the output factors of small electron fields,  $d_{\max}$  values should be observed by film dosimetry [11].

#### 4. Conclusion

The dosimetry of small electron fields is highly critical. Output measurements of electron fields smaller than the extent of the lateral scatter equilibrium must be carefully made using appropriate dosimetry. Furthermore, for the

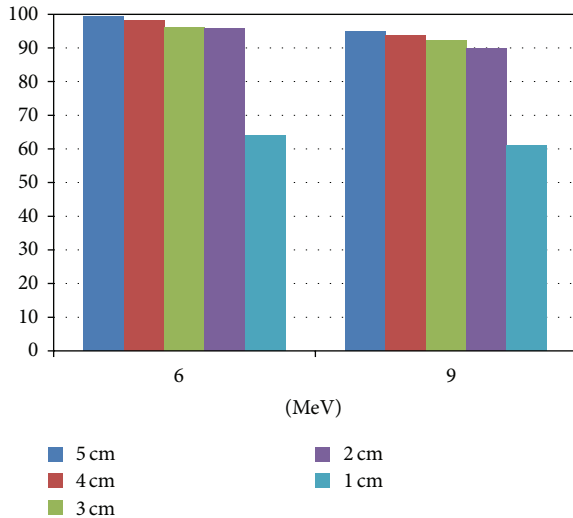


FIGURE 6: Gamma analysis results for beams with 6 and 9 MeV energy, for cut-out diameters of 4, 3, 2, and 1 cm using a 5 cm circular cone at 100 cm SSD ( $y$ -axis is %).

patient-time calculation, output factors that were obtained by the most appropriate dosimetric method should be used, not the values from the TPS that uses the pencil beam algorithm.

At the conclusion of this study, it was observed that in the CMS XiO TPS, calculated using the pencil beam algorithm, the dose distributions of electron treatment fields that were created with circular cut-outs of 4, 3, and 2 cm diameter were appropriate for patient treatment, but those created using a 1 cm diameter field were not. Additionally, the pencil beam algorithm is not convenient for MU calculations in electron dosimetry.

## Conflict of Interests

The authors declare that there is no conflict of interests regarding the publication of this paper.

## References

- [1] E. B. Podgorsak, *Radiation Oncology Physics: a Handbook for Teachers and Students*, International Atomic Energy Agency, Vienna, Austria, 2005.
- [2] J. Cassidy, D. Bisset, and R. Obe, *Oxford Handbook of Oncology*, Oxford University Press, New York, NY, USA, 2002.
- [3] E. Sternick, "Algorithms for computerized treatment planning," in *Practical Aspects of Electron Beam Treatment Planning: Proceedings of the Practical Aspects of Electron Beam Treatment Planning Symposium, July 31, 1977, Cincinnati, Ohio, New York*, C. G. Orton and F. Baagne, Eds., p. 52, American Institute of Physics, 1978.
- [4] S. C. Sharma, D. L. Wilson, and B. Jose, "Dosimetry of small fields for Therac 20 electron beams," *Medical Physics*, vol. 11, no. 5, pp. 697–702, 1984.
- [5] K. R. Hogstrom, G. Starkschall, and A. S. Shiu, "Dose calculation algorithms for electron beams," in *Advances in Radiation Oncology Physics: Dosimetry, Treatment Planning and*

*Brachytherapy*. American Institute of Physics Monograph, J. A. Purdy, Ed., p. 900, American Institute of Physics, New York, NY, USA, 1992.

- [6] H. Bilge, N. Ozbek, M. Okutan, A. Cakir, and H. Acar, "Surface dose and build-up region measurements with wedge filters for 6 and 18 MV photon beams," *Japanese Journal of Radiology*, vol. 28, no. 2, pp. 110–116, 2010.
- [7] ISP International Speciality Products, "Gafchromic EBT Self-Developing Film for Radiotherapy Dosimetry," 2007, [http://online1.ispcorp.com/\\_layouts/Gafchromic/content/products/ebt/pdfs/EBTwhitepaper.pdf](http://online1.ispcorp.com/_layouts/Gafchromic/content/products/ebt/pdfs/EBTwhitepaper.pdf).
- [8] D. A. Low, W. B. Harms, S. Mutic, and J. A. Purdy, "A technique for the quantitative evaluation of dose distributions," *Medical Physics*, vol. 25, no. 5, pp. 656–661, 1998.
- [9] D. A. Low and J. F. Dempsey, "Evaluation of the gamma dose distribution comparison method," *Medical Physics*, vol. 30, no. 9, pp. 2455–2464, 2003.
- [10] IAEA, "Absorbed dose determination in external beam radiotherapy: an international code of practice for dosimetry based on standards of absorbed dose to water," Tech. Rep. 398, International Atomic Energy Agency, 2000.
- [11] S. C. Sharma, M. W. Johnson, and M. S. Gossman, "Practical considerations for electron beam small field size dosimetry," *Medical Dosimetry*, vol. 30, no. 2, pp. 104–106, 2005.
- [12] Z. Xu, S. E. Walsh, T. P. Telivala, A. G. Meek, and G. Yang, "Evaluation of the eclipse electron Monte Carlo dose calculation for small fields," *Journal of Applied Clinical Medical Physics*, vol. 10, no. 3, pp. 75–85, 2009.
- [13] F.-C. Su, Y. Liu, S. Stathakis, C. Shi, C. Esquivel, and N. Papanikolaou, "Dosimetry characteristics of Gafchromic EBT film responding to therapeutic electron beams," *Applied Radiation and Isotopes*, vol. 65, no. 10, pp. 1187–1192, 2007.

## Research Article

# Detection Efficiency of NaI(Tl) Detector in 511–1332 keV Energy Range

I. Akkurt,<sup>1</sup> K. Gunoglu,<sup>2</sup> and S. S. Arda<sup>1</sup>

<sup>1</sup> Fen-Edebiyat Fakültesi Fizik Böl, Suleyman Demirel University, 32260 Isparta, Turkey

<sup>2</sup> Teknisk Bil. MYO, Suleyman Demirel University, 32260 Isparta, Turkey

Correspondence should be addressed to I. Akkurt; [iskenderakkurt@sdu.edu.tr](mailto:iskenderakkurt@sdu.edu.tr)

Received 13 August 2013; Revised 9 December 2013; Accepted 15 December 2013; Published 12 March 2014

Academic Editor: Jakrapong Kaewkhao

Copyright © 2014 I. Akkurt et al. This is an open access article distributed under the Creative Commons Attribution License, which permits unrestricted use, distribution, and reproduction in any medium, provided the original work is properly cited.

As it is important to obtain accurate analytical result in an experimental research, this required quality control of the experimental system. Gamma spectrometry system can be used in a variety of different fields such as radiation and medical physics. In this paper the absolute efficiency, peak to valley ratio, and energy resolution of a 3'' × 3'' NaI(Tl) detector were determined experimentally for 511, 662, 835, 1173, 1275, and 1332 keV photon energies obtained from <sup>22</sup>Na, <sup>54</sup>Mn, <sup>60</sup>Co, and <sup>137</sup>Cs radioactive sources.

## 1. Introduction

With the start of using radioactive sources in a variety of different fields such as health physics, industry, energy, and environmental application nuclear radiation detectors become the most fundamental instruments as radiation is hazardous for health. In a radiation measurement an accurate knowledge of the detector spectral performance is required. As the radiation can travel large distances between the interactions in the detector material before detection is possible, the detectors do not have 100% efficiency. In the radiation measurement, one of the most important characteristics of a detector is the efficiency of the detector. Gamma spectrometry is one of the most widely used detector systems in this field and its performance directly depends on the knowledge of the detection efficiency. The detection efficiency is a measure of the percentage of radiation that a given detector detects from the overall yield emitted from the source. It can vary with the volume and shape of the detector material, absorption cross-section in the material, attenuation layers in front of the detector, and distance and position from the source to the detector [1].

Detection efficiency of a detector system depends on different parameters and thus various kinds of the efficiency definitions are used to cover those parameters.

- (i) Absolute efficiency: it is the ratio of the number of counts recorded by the detector to the number of gamma rays emitted by the source (in all directions).
- (ii) Intrinsic efficiency: it is the ratio of the number of pulses recorded by the detector to the number of gamma rays hitting the detector.
- (iii) Full-energy peak (or photopeak) efficiency: it is the efficiency for producing full-energy peak pulses only, rather than a pulse of any size, for the gamma ray.

Especially in the radioactivity measurement the absolute efficiency of the detector must be known. It is defined as the ratio of the number of counts recorded by the detector ( $N_c$ ) to the number of radiation ( $N_s$ ) emitted by the source (in all directions) as represented in the following formula:

$$\varepsilon_{\text{abs}} = \frac{N_c}{N_s}. \quad (1)$$

Absolute efficiency of the detector depends not only on detector properties but also on the details of the counting geometry.

Various experimental and calculation works have been reported for the detection efficiency work [2–6].

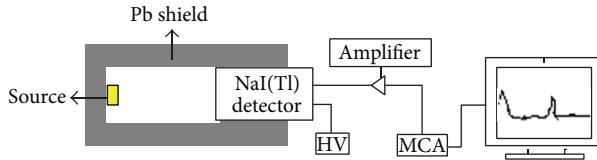


FIGURE 1: Schematic view of the experimental system.

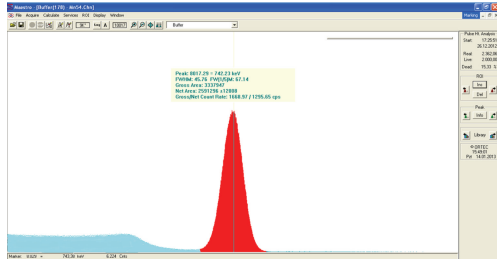
FIGURE 2: Gamma ray spectrum obtained from  $^{137}\text{Cs}$  source.

TABLE 1: The present activity and half-life of the radioactive sources used to obtain energies.

Nuclide	Activity (micro Ci)	Half-life (day)
$^{22}\text{Na}$	0.706	950.8
$^{54}\text{Mn}$	0.348	312.3
$^{137}\text{Cs}$	0.970	11020.0
$^{60}\text{Co}$	0.843	1925.5

For the gamma ray spectrometry, the absolute efficiency and energy resolution are important parameters to be determined. Those parameters are usually done using a function to fit the efficiency at a wide energies range, as the number of energy peaks obtained from radioactive sources is limited. For these purposes the absolute efficiency and the energy resolution of the NaI(Tl) detector have been determined experimentally at 511, 662, 835, 1173, 1275, and 1332 keV energies obtained from  $^{22}\text{Na}$ ,  $^{54}\text{Mn}$ ,  $^{60}\text{Co}$ , and  $^{137}\text{Cs}$  radioactive isotopes.

## 2. Experimental Methods

The gamma ray spectrometry consists of a  $3 \times 3''$  NaI(Tl) detector and this is connected to 16384-channel Multichannel Analyser (MCA). The spectrum obtained from MCA is analyzed using the Genie 2 software obtained from Canberra [7–9]. In order to reduce the background level of the system, the detector is shielded using 6 cm lead on all sides. A schematic view of the system has been displayed in Figure 1. The 4 different radiation sources ( $^{22}\text{Na}$ ,  $^{54}\text{Mn}$ ,  $^{60}\text{Co}$ , and  $^{137}\text{Cs}$ ) that give 511, 662, 835, 1173, 1275, and 1332 keV gamma ray energy were placed at 5 different distances (0,5, 1, 3, 5, and 10 cm) from the face of detector and the measurement has been performed for each source. Each measurement has been done for a period of 60 min to obtain good statistics in the evaluation of each gamma peak. Typical gamma ray spectrum for  $^{137}\text{Cs}$  and  $^{60}\text{Co}$  sources taken with the NaI(Tl) detector is given in Figures 2 and 3. In Table 1 the present activity

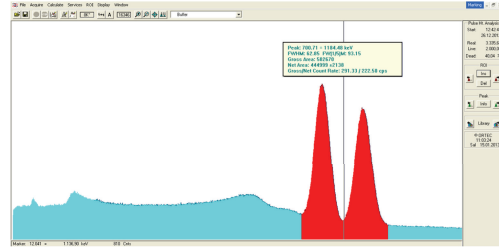
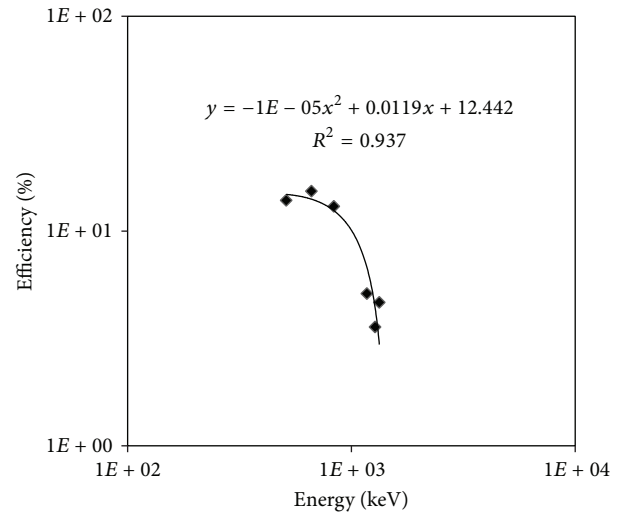
FIGURE 3: Gamma ray spectrum obtained from  $^{60}\text{Co}$  source.

FIGURE 4: Detection efficiency of NaI(Tl) detector as a function of gamma ray energies (source placed at 0,5 cm distance to the detector face).

TABLE 2: The energies and emission probabilities of the radioisotope source [11].

Nuclide	Energy (keV)	Emission probability (%)
$^{22}\text{Na}$	511.00	178.00
	1274.60	99.94
$^{54}\text{Mn}$	834.83	85.59
$^{137}\text{Cs}$	661.66	85.30
$^{60}\text{Co}$	1173.23	99.85
	1332.48	99.98

and half-life of the radioisotope sources are given and in Table 2 the energies and emission probabilities of the radioisotope source are given.

## 3. Results and Discussions

The properties such as detector efficiency, energy calibration, and energy resolution of a NaI(Tl) detector have been measured for 6 different gamma ray energies.

**3.1. Efficiency Calibrations.** The detection efficiency of the NaI(Tl) detector was obtained using (1) for each gamma ray energy emitted by the  $^{22}\text{Na}$ ,  $^{54}\text{Mn}$ ,  $^{60}\text{Co}$ , and  $^{137}\text{Cs}$  radioactive

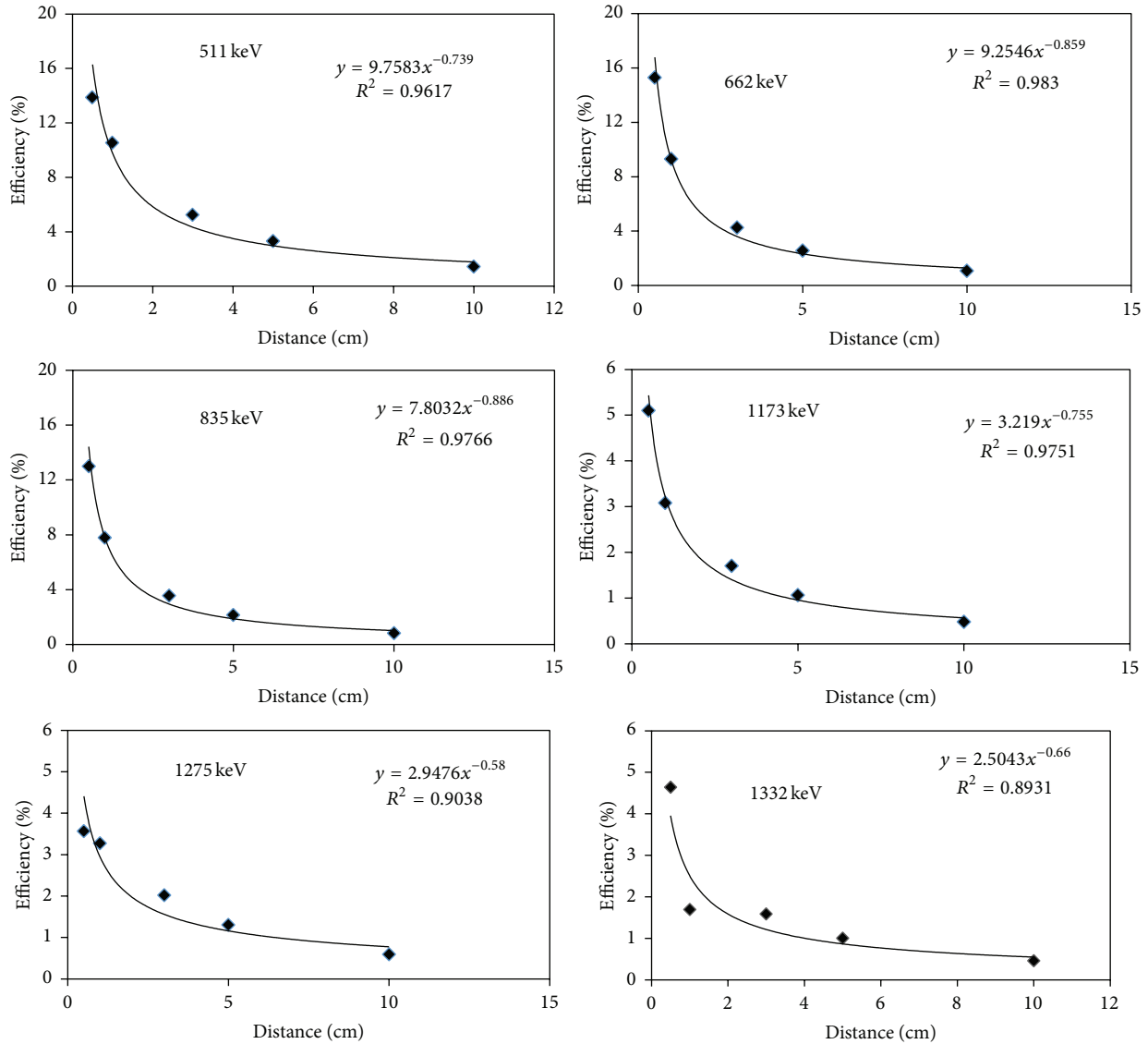


FIGURE 5: Variation of detection efficiency of NaI(Tl) detector as a function of distance.

isotopes. The obtained results have been displayed as a function of gamma ray energy in Figure 4. As can be seen from this figure, there is a great variety of analytical functions that is used to describe the efficiency dependence on the energy. The solid line represents a second degree polynomial fit that gives a good description with the correlation coefficient between the efficiency values and the gamma ray energies, which is about  $R^2 = 0,94$ .

As the detection efficiency of the NaI(Tl) detector can vary with the distance to the detector face, the efficiencies have been obtained for 5 different distances from the detector. The results are displayed in Figure 5 for 5 different distances and 6 different energies. It can be seen from this figure that the detection efficiency has decreased exponentially with the increasing distance from detector face.

The obtained results have been compared with the calculation obtained using the same detector size [10].

The comparisons have been displayed in Figures 6 and 7 where 0.5 and 10 cm distances have been used. A good agreement between experimental and calculated results was obtained as can be seen from these figures.

**3.2. Energy Calibrations and Resolution.** The detector system should be calibrated before using in radiation detection in order to covert channel number to energy scale. This is carried out under laboratory conditions that mimic as closely as possible the experimental conditions. Several radioactive sources (at least 3 different energy peaks) are used to get certain peak to see channel number. This is usually done using <sup>137</sup>Cs and <sup>60</sup>Co radioactive sources as they produce  $\gamma$ -ray energy of 662, 1170, and 1332 keV, respectively. In Figure 8 the  $\gamma$ -ray spectrum obtained from those sources and related fit has been displayed.

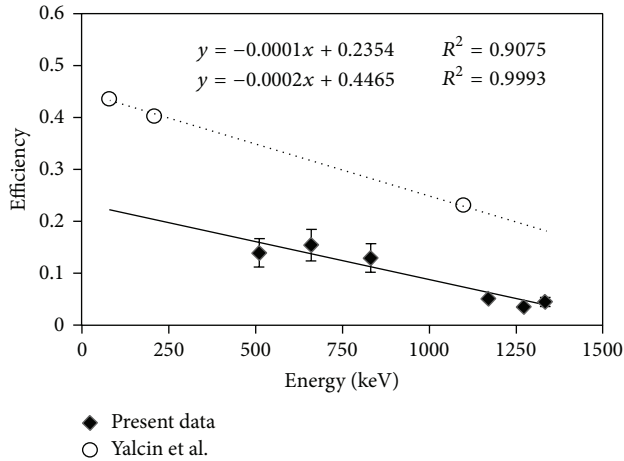


FIGURE 6: Comparison of measured and calculated detection efficiency of NaI(Tl) detector (source placed at 0,5 cm distance to the detector face).

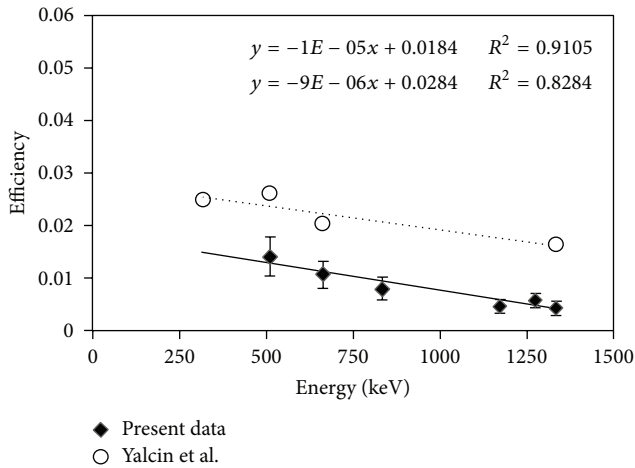


FIGURE 7: Comparison of measured and calculated detection efficiency of NaI(Tl) detector (source placed at 10 cm distance to the detector face).

The energy resolution of a detector system is obtained from the peak full width at one-half of the maximum height (FWHM) of a single peak using the following equation:

$$R = \frac{\text{FWHM}}{E_0} \times 100. \quad (2)$$

Here  $R$  is energy resolution and  $E_0$  is the related energy. It will provide the separation for two adjacent energy peaks which will lead to identification of different nuclide in spectrum. The measured energy resolution of the NaI(Tl) detector is displayed in Figure 9 as a function of gamma ray energy. It can be seen from this figure that the energy resolution of the NaI(Tl) detector decreased with the FWHM with the increasing gamma ray energy.

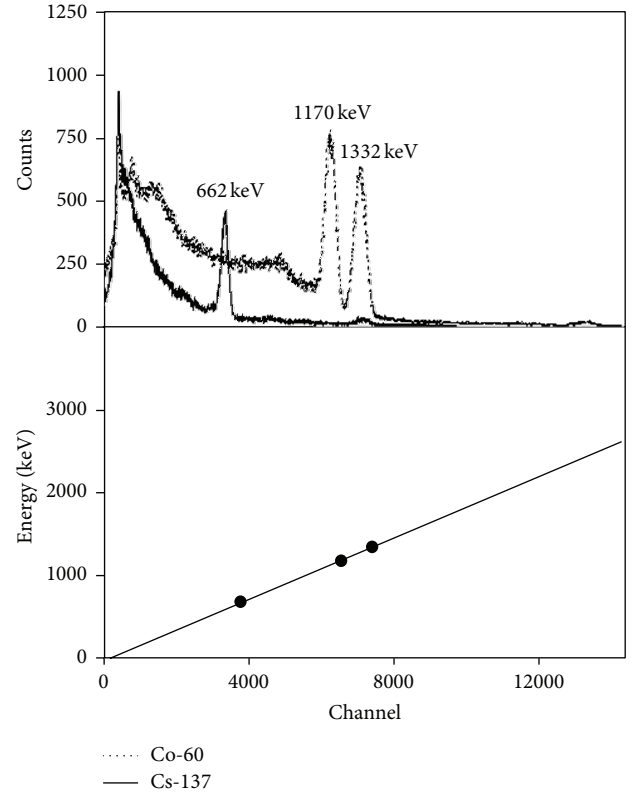


FIGURE 8: Energy spectrum and calibration fit for  $^{137}\text{Cs}$  and  $^{60}\text{Co}$  sources.

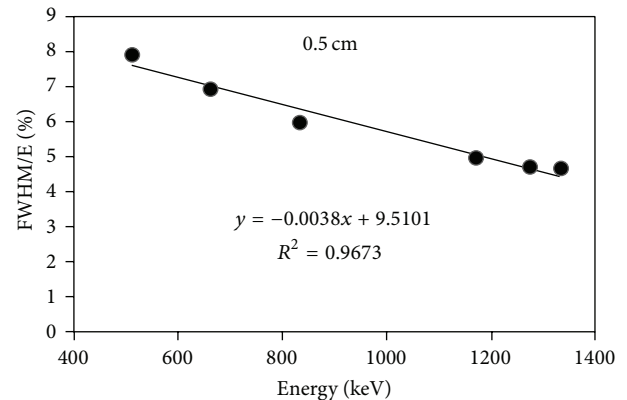


FIGURE 9: Energy resolution of the NaI(Tl) detector obtained for 0,5 cm distance.

## 4. Conclusions

The detection efficiency and energy resolution for the NaI(Tl) scintillation detectors were measured. The variation of detection efficiency with the gamma ray energy and detection distance was also investigated. It was found from this work that the detection efficiency depends on gamma ray energy and also source distance to the detector.

## Conflict of Interests

The authors declare that there is no conflict of interests regarding the publication of this paper.

## Acknowledgments

This work has been supported partly by the Suleyman Demirel University Foundation Unit (3312-YL2-12) and partly by the State Planning Unit (DPT2006K-120470) in Turkey.

## References

- [1] K. Debertin and R. G. Helmer, *Gamma- and X-Ray Spectrometry with Semiconductor Detectors*, North-Holland, 1988.
- [2] L. Zikovsky and B. Chah, "A computer program for calculating Ge(Li) detector counting efficiencies with large volume samples," *Nuclear Instruments and Methods in Physics Research A*, vol. 263, no. 2-3, pp. 483–486, 1988.
- [3] Y. S. Selim, M. I. Abbas, and M. A. Fawzy, "Analytical calculation of the efficiencies of gamma scintillators—part I: total efficiency for coaxial disk sources," *Radiation Physics and Chemistry*, vol. 53, no. 6, pp. 589–592, 1998.
- [4] A. Jehouani, R. Ichaoui, and M. Boulkheir, "Study of the NaI(Tl) efficiency by Monte Carlo method," *Applied Radiation and Isotopes*, vol. 53, no. 4-5, pp. 887–891, 2000.
- [5] M. I. Abbas, "Analytical formulae for well-type NaI (Tl) and HPGe detectors efficiency computation," *Applied Radiation and Isotopes*, vol. 55, no. 2, pp. 245–252, 2001.
- [6] A. Gültekin, G. Kaynak, and O. Gürler, "Determination of full energy peak efficiency of HpGe detector from 59.5 to 1332.5 keV," *Indian Journal of Pure and Applied Physics*, vol. 44, no. 4, pp. 281–286, 2006.
- [7] I. Akkurt and H. Akyıldırım, "Radiation transmission of concrete including pumice for 662, 1173 and 1332 keV gamma rays," *Nuclear Engineering and Design*, vol. 252, pp. 163–166, 2012.
- [8] I. Akkurt and A. Alkhayatt, "The effect of barite proportion on neutron and gamma-ray shielding," *Annals of Nuclear Energy*, vol. 51, pp. 5–9, 2013.
- [9] B. Mavi and I. Akkurt, "Natural radioactivity and radiation hazards in some building materials used in Isparta, Turkey," *Radiation Physics and Chemistry*, vol. 79, no. 9, pp. 933–937, 2010.
- [10] S. Yalcin, O. Gurler, G. Kaynak, and O. Gundogdu, "Calculation of total counting efficiency of a NaI(Tl) detector by hybrid Monte-Carlo method for point and disk sources," *Applied Radiation and Isotopes*, vol. 65, no. 10, pp. 1179–1186, 2007.
- [11] R. B. Firestone and L. P. Ekström, "Table of Radioactive Isotopes; Database Version 2.1.," 2004, <http://ie.lbl.gov/toi/>.

## Research Article

# Radiation Shielding Properties Comparison of Pb-Based Silicate, Borate, and Phosphate Glass Matrices

**Suwimon Ruengsri**

*Chemistry Program, Faculty of Science and Technology, Nakhon Pathom Rajabhat University, Nakhon Pathom 73000, Thailand*

Correspondence should be addressed to Suwimon Ruengsri; [suwimonn@live.com](mailto:suwimonn@live.com)

Received 5 December 2013; Accepted 4 January 2014; Published 23 February 2014

Academic Editor: Jakrapong Kaewkhao

Copyright © 2014 Suwimon Ruengsri. This is an open access article distributed under the Creative Commons Attribution License, which permits unrestricted use, distribution, and reproduction in any medium, provided the original work is properly cited.

Theoretical calculations of mass attenuation coefficients, partial interactions, atomic cross-section, and effective atomic numbers of PbO-based silicate, borate, and phosphate glass systems have been investigated at 662 keV. PbO-based silicate glass has been found with the highest total mass attenuation coefficient and then phosphate and borate glasses, respectively. Compton scattering has been the dominate interaction contributed to the different total attenuation coefficients in each of the glass matrices. The silicate and phosphate glass systems are more appropriate choices as lead-based radiation shielding glass than the borate glass system. Moreover, comparison of results has shown that the glasses possess better shielding properties than standard shielding concretes, suggesting a smaller size requirement in addition to transparency in the visible region.

## 1. Introduction

The interaction of high-energy photons with matter is important in radiation medicine and biology, nuclear engineering, and space technology. Glass has double functions of being transparent to visible light and absorbing gamma rays and neutrons, thus, providing a radiation shielding for observers or experimenters. It may also be mentioned that verifications are an interesting option for long-term storage of radioactive waste products [1].

Nowadays, the existing dense silicate flints and their radiation-resistant analogs are characterized by an insufficiently high radiation-optical resistance, a yellowness as a result of a low transmission in the blue and near-UV spectral ranges, high melting temperatures, and a low optical homogeneity due to the corrosive interaction of melts with refractory used for fabricating crucibles and other units of production accessories of a melting facility. This limits the possibility of using radiation-resistant silicate flints for manufacturing radiation-shielding viewing windows for so-called “hot” chambers, medical or industrial radiation facilities, and nuclear and chemical reconnaissance vehicles. Although the existing dense silicate flints have long been manufactured on a commercial scale, it was necessary to design the composition

of a new glass that should be transparent over a wider spectral range and have radiation-optical resistance and radiation-shielding properties, at least, no worse than similar characteristics of the existing silicate flints [2].

During the last two decades, borate and phosphate glasses have been investigated extensively, yet there is still a great interest in developing new glasses suited for the demands of both industry and technology. Borate glasses have the promising application for the metal-ceramic seals for their lowing melting temperature and high thermal expansion coefficient matching with that of metals. In such applications, it is found that the glass does not bond directly to the metal but to an oxide that is conventionally formed by a thermal treatment on the metal prior to bonding. The resulting oxide acts as a bonding agent in that it is bonded to the underlying metal and the glass material [3]. In any case, phosphate glasses have low glass transition temperatures, low optical dispersions, and relatively high thermal expansion coefficients [4, 5]. Furthermore, the poor chemical durability, high hygroscopic, and volatile nature of phosphate glasses prevented them from replacing the conventional glasses in a wide range of technological applications. These properties make them useful candidates for fast ion conducting material, biomedical application, and biocompatible materials, such as

bone regeneration application [6] and shielding materials [7]. However, the reports of phosphate glass in radiation shielding glass are very limited. Arbuzov and Fyodorov [7] studied optical, spectral, and radiation shielding properties of high lead phosphate glasses.

Good reviews on radiation shielding glass development have been published recently by several authors for several glass matrices, silicate glass [8], borate glass [9–11], and phosphate glass [2, 7]. In this work, we have calculated the mass attenuation coefficients, the partial interaction, and the effective atomic numbers of silicate, borate, and phosphate glass containing PbO at 662 keV, using WinXCom software. The comparisons of radiation shielding properties between glass matrices are also discussed. The glass formulas in this study are  $x\text{PbO}:(100-x)\text{SiO}_2$ ,  $x\text{PbO}:(100-x)\text{B}_2\text{O}_3$ , and  $x\text{PbO}:(100-x)\text{P}_2\text{O}_5$ , where  $x$  is varied from 30 to 70% by weight.

## 2. Theory and Method

In this section, we summarize theoretical relations used in the present work. The total probability for interaction  $\mu$ , called the total linear ( $\mu$ ) attenuation coefficient, is equal to the sum of the partial probabilities [12]:

$$\mu = \tau + \sigma + \kappa, \quad (1)$$

where  $\tau$ ,  $\sigma$ , and  $\kappa$  are the probability for photoelectric absorption, Compton scattering, and pair production, respectively, and can be derived from the following formula [12]:

$$\begin{aligned} \tau \text{ (cm}^{-1}\text{)} &= aN \left( \frac{Z^n}{E_\gamma^m} \right) [1 - f(Z)], \\ \sigma \text{ (cm}^{-1}\text{)} &= NZf(E_\gamma), \\ \kappa \text{ (cm}^{-1}\text{)} &= NZ^2f(E_\lambda, Z), \end{aligned} \quad (2)$$

in which  $a$  is a constant coefficient, independent of  $Z$  and  $E_\gamma$ . Parameters  $m$  and  $n$  are constants with values between 3 and 5 depending on gamma energy.  $N$  is atomic density and  $Z$  is atomic number. Although the coherent scattering can appear, but it has very tiny influence at high energy. Theoretical values of the mass attenuation coefficients ( $\mu_m$ ) of mixture or compound have been calculated by WinXCom, based on the mixture rule [13]. Thus

$$\frac{\mu}{\rho} = \mu_m = \sum_i^n w_i(\mu_m)_i, \quad (3)$$

where  $(\mu_m)_i$  is the mass attenuation coefficient for the individual element in each component and  $w_i$  is the fractional weight of the element in each component. This mixture is valid when the effects of molecular binding and chemical and crystalline environments are negligible. Theoretical values for the mass attenuation coefficient can be found in the tabulation by Hubbell and Seltzer. A lot of manual work can be saved by using suitable software. Berger and Hubbell developed XCOM for calculating mass attenuation coefficients or photon interaction cross-sections for any element, compound, or

TABLE 1: Total mass attenuation coefficients of PbO containing silicate, borate, and phosphate glass systems at 662 keV.

PbO composition (wt%)	$\mu_m (\times 10^{-2} \text{ cm}^2/\text{g})$		
	Silicate glass	Borate glass	Phosphate glass
30	8.64	8.51	8.58
40	8.95	8.84	8.89
50	9.25	9.16	9.21
60	9.56	9.48	9.52
70	9.86	9.81	9.83

mixture at energy from 1 KeV to 100 GeV. Recently, XCOM was transformed to the Windows platform by Gerward et al. [14], called WinXCom.

WinXCom can generate cross-section or attenuation coefficients of element, mixture, and compound on a standard energy grid, spaced approximately logarithmically, on a grid specified by the user, or for a mix of both grids. The program provides total cross-sections and attenuation coefficients as well as partial cross-section for incoherent and coherent scattering, photoelectric absorption, and pair production. For compound, the quantities calculated are partial and total mass attenuation coefficients. Total attenuation coefficients without the contribution from coherent scattering are also given, since they are often used in gamma-rays transport calculation [15].

## 3. Results and Discussion

The total mass attenuation coefficients of the three PbO containing glass systems are shown in Table 1. From the table, the total mass attenuation coefficients of PbO-based silicate glass are higher than in phosphate and borate glasses, respectively, showing that photons are more attenuated in silicate glass than the other two glasses. It was found that the total mass attenuation coefficients were increased with increasing PbO concentration in all glass systems as shown in Table 2. This is due to increasing of interactions via photoelectric absorption in glass samples. The increasing rate and values of photoelectric absorption in all glass systems are comparable and proportional with PbO content.

The variation of Compton scattering with PbO concentration in all glass systems is shown in Figure 1; the Compton scattering decreases with increasing PbO concentration. The decreasing rates of Compton interaction in all glass systems are comparable. The Compton scattering in silicate glass shows the highest in value and then phosphate and borate glass, respectively, reflecting that photons are better scattered in silicate glass at this energy. Moreover, Table 2 shows that in all the glass systems, Compton scattering is a dominate interaction process in this work. These results are explained with total mass attenuation values. While the coherent scattering has only weak effect on the total mass attenuation coefficients for all glass systems, the pair production interaction does not occur because the energy is lower than 1.02 MeV. This work has been in good agreement with experimental works by Kirdsiri et al. [16], Singh et al. [11], and Singh et al. [8] in

TABLE 2: Partial interaction of PbO containing silicate, borate, and phosphate glass systems at 662 keV.

PbO composition (wt%)	Silicate glass	Borate glass	Phosphate glass
Photoelectric interaction at 662 keV ( $\times 10^{-2}$ cm <sup>2</sup> /g)			
30	1.21	1.21	1.21
40	1.61	1.61	1.61
50	2.01	2.01	2.01
60	2.42	2.41	2.42
70	2.82	2.82	2.82
Compton interaction at 662 keV ( $\times 10^{-2}$ cm <sup>2</sup> /g)			
30	7.23	7.11	7.16
40	7.07	6.97	7.01
50	6.92	6.83	6.87
60	6.76	6.69	6.72
70	6.60	6.55	6.57
Coherent interaction at 662 keV ( $\times 10^{-2}$ cm <sup>2</sup> /g)			
30	0.20	0.19	0.20
40	0.26	0.26	0.26
50	0.32	0.32	0.32
60	0.38	0.38	0.38
70	0.44	0.44	0.44

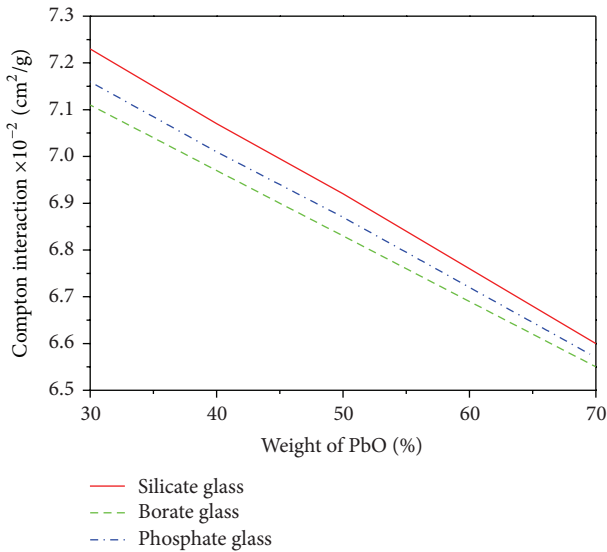


FIGURE 1: The Compton scattering interaction of PbO containing silicate, borate, and phosphate glass systems at 662 keV.

the case of lead borate, bismuth borate, and lead silicate glass systems, respectively. All of partial interaction data are shown in Table 2 along with their PbO concentrations.

**3.1. Cross-Sections and Effective Atomic Numbers.** In this section, the total atomic cross-section,  $\sigma_{t,a}$ , can be expressed as

$$\sigma_{t,a} = \frac{1}{N_A} \sum_i f_i A_i \mu_{m,i}, \quad (4)$$

where  $f_i$  is the fractional abundance of element  $i$  with respect to number of atoms,  $A_i$  is the atomic weight of element  $i$ , and  $N_A$  is the Avogadro constant. Similarly to the total electronic cross-section,  $\sigma_{t,e}$ , is expressed by the following formula:

$$\sigma_{t,e} = \frac{1}{N_A} \sum_i f_i \frac{A_i}{Z_i} \mu_{m,i}. \quad (5)$$

The total atomic and electronic cross-sections are related to the effective atomic number,  $Z_{\text{eff}}$ , through the following relation:

$$Z_{\text{eff}} = \frac{\sigma_{t,a}}{\sigma_{t,e}}. \quad (6)$$

The atomic cross-section and the effective atomic number of the glasses are shown in Table 3. The results show that the effective atomic numbers were increased with increasing of PbO concentration in all glass systems. It is due to the increasing of photoelectric absorption; as with theoretical approach, the photoelectric absorption depends on atomic number while on the other hand the Compton scattering tends to depend on density [17]. The effective atomic numbers of borate glass are lower than silicate and phosphate glass, respectively; as shown in Figure 2, this is due to lower atomic cross-section as shown in Table 3. The results are supported by experimental data from Kirdsiri et al. [16]. Figure 3 shows the comparison of mass attenuation coefficients between the glass systems and two concrete systems (ordinary concrete and barite concrete) [10]. It has been observed that all glass systems can obtain better shielding properties than the two concretes for all PbO concentrations, reflecting that the PbO containing glasses can be very useful as radiation shielding materials.

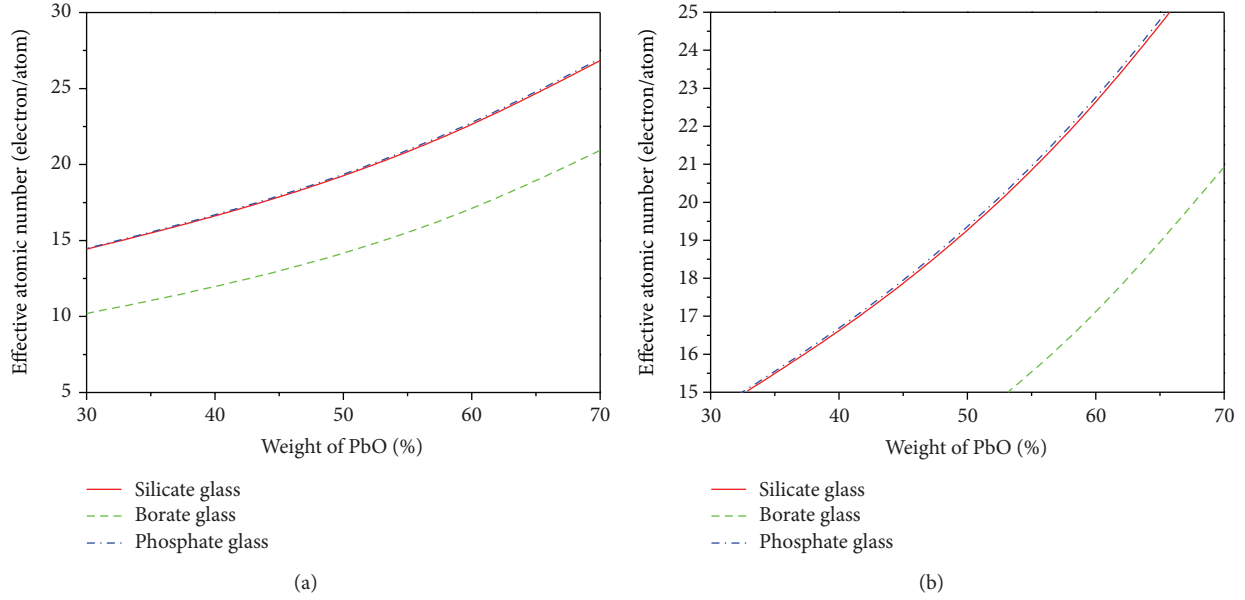


FIGURE 2: (a) The effective atomic numbers of PbO containing silicate, borate, and phosphate glass systems at 662 keV; (b) expansion view of (a).

TABLE 3: Total atomic cross-sections and effective atomic numbers of PbO containing silicate, borate, and phosphate glass system at 662 keV.

Composition of PbO (wt%)	$\sigma_{t,at}$ (b/atom)		
	Silicate glass	Borate glass	Phosphate glass
30	3.81	2.67	3.83
40	4.43	3.15	4.45
50	5.22	3.77	5.25
60	6.26	4.62	6.30
70	7.71	5.86	7.75

Composition of PbO (wt%)	$Z_{eff}$ (electron/atom)		
	Silicate glass	Borate glass	Phosphate glass
30	14.43	10.20	14.48
40	16.54	11.89	16.61
50	19.15	14.06	19.24
60	22.47	16.93	22.59
70	26.84	20.93	26.97

Furthermore, the results suggested that silicate and phosphate glass systems are more appropriate than borate glass system as lead-based radiation shielding glass.

#### 4. Conclusion

In this work, the mass attenuation coefficients, partial interactions, atomic cross-section, and the effective atomic numbers of silicate, borate, and phosphate glass systems containing PbO have been investigated. It has been found that silicate and phosphate glass systems are more appropriate than borate glass system in the case of lead-based radiation shielding

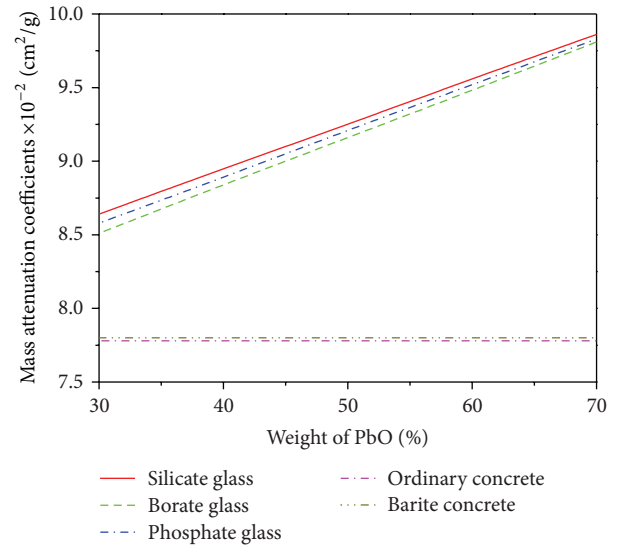


FIGURE 3: The mass attenuation coefficients of PbO containing silicate, borate, and phosphate glass systems at 662 keV in comparison with two shielding concretes.

glass. However, each glass system may be used depending on the intended application and experimental rechecks which are vital. Our results showed that the glasses are potential candidates for gamma-rays shielding materials. They exhibited with better values of shielding properties in comparison with some standard shielding concretes. This suggested a smaller size requirement in addition to transparency in the visible region.

Further investigations on the photon absorption in the glass materials are in progress, especially on other theoretical

treatments such as X-ray form factor, attenuation, and scattering table (FFAST) [18, 19] to establish uncertainties estimation for better reliability of the results.

### Conflict of Interests

The author declares that there is no conflict of interests regarding the publication of this paper.

### Acknowledgment

The author would like to thank Nakhon Pathom Rajabhat University (NPRU) for partially supporting this paper.

### References

- [1] S. R. Manohara, S. M. Hanagodimath, and L. Gerward, "Photon interaction and energy absorption in glass: a transparent gamma ray shield," *Journal of Nuclear Materials*, vol. 393, no. 3, pp. 465–472, 2009.
- [2] V. I. Arbuzov, N. Z. Andreeva, N. A. Leko, S. I. Nikitina, N. F. Orlov, and Y. K. Fedorov, "Optical, spectral, and radiation-shielding properties of high-lead phosphate glasses," *Glass Physics and Chemistry*, vol. 31, no. 5, pp. 583–590, 2005.
- [3] D. Zhu, X. Lou, F. Luo, L. Xiong, and W. Zhou, "Electronic structure and physical properties of hcp  $Ti_3Al$  type alloys," *Transactions of Nonferrous Metals Society of China*, vol. 17, no. 4, pp. 766–771, 2007.
- [4] G. L. Flower, G. S. Baskaran, M. S. Reddy, and N. Veeraiiah, "The structural investigations of  $PbO-P_2O_5-Sb_2O_3$  glasses with  $MoO_3$  as additive by means of dielectric, spectroscopic and magnetic studies," *Physica B*, vol. 393, no. 1-2, pp. 61–72, 2007.
- [5] H. Doweidar, Y. M. Moustafa, K. El-Egili, and I. Abbas, "Infrared spectra of  $Fe_2O_3-PbO-P_2O_5$  glasses," *Vibrational Spectroscopy*, vol. 37, no. 1, pp. 91–96, 2005.
- [6] L. D. Burling, *Novel phosphate glasses for bone. Regeneration applications [Ph.D. thesis]*, University of Nottingham, 2005.
- [7] V. I. Arbuzov and Y. K. Fyodorov, "Spectral, radiation-optical and shielding properties of phosphate glasses with high lead content," *Advanced Materials Research*, vol. 39-40, pp. 213–218, 2008.
- [8] K. J. Singh, N. Singh, R. S. Kaundal, and K. Singh, "Gamma-ray shielding and structural properties of  $PbO-SiO_2$  glasses," *Nuclear Instruments and Methods in Physics Research B*, vol. 266, no. 6, pp. 944–948, 2008.
- [9] N. Singh, K. J. Singh, K. Singh, and H. Singh, "Gamma-ray attenuation studies of  $PbO-BaO-B_2O_3$  glass system," *Radiation Measurements*, vol. 41, no. 1, pp. 84–88, 2006.
- [10] N. Singh, K. J. Singh, K. Singh, and H. Singh, "Comparative study of lead borate and bismuth lead borate glass systems as gamma-radiation shielding materials," *Nuclear Instruments and Methods in Physics Research B*, vol. 225, no. 3, pp. 305–309, 2004.
- [11] K. Singh, H. Singh, V. Sharma et al., "Gamma-ray attenuation coefficients in bismuth borate glasses," *Nuclear Instruments and Methods in Physics Research B*, vol. 194, no. 1, pp. 1–6, 2002.
- [12] M. Jalali and A. Mohammadi, "Gamma ray attenuation coefficient measurement for neutron-absorbent materials," *Radiation Physics and Chemistry*, vol. 77, no. 5, pp. 523–527, 2008.
- [13] D. F. Jackson and D. J. Hawkes, "X-ray attenuation coefficients of elements and mixtures," *Physics Reports*, vol. 70, no. 3, pp. 169–233, 1981.
- [14] L. Gerward, N. Guilbert, K. Bjorn Jensen, and H. Levring, "X-ray absorption in matter. Reengineering XCOM," *Radiation Physics and Chemistry*, vol. 60, no. 1-2, pp. 23–24, 2001.
- [15] L. Gerward, N. Guilbert, K. B. Jensen, and H. Levring, "WinXCom—a program for calculating X-ray attenuation coefficients," *Radiation Physics and Chemistry*, vol. 71, no. 3-4, pp. 653–654, 2004.
- [16] K. Kirdsiri, J. Kaewkhaob, A. Pokaipisitc, W. Chewpraditkula, and P. Limsuwana, "Gamma-rays shielding properties of  $xPbO:(100-x)B_2O_3$  glasses system at 662 keV," *Annals of Nuclear Energy*, vol. 36, no. 9, pp. 1360–1365, 2009.
- [17] N. Tsoulfaniidis, *Measurement and Detection of Radiation*, pp. 144–147, Hemisphere Publishing, Washington, DC, USA; McGraw-Hill, New York, NY, USA, 1983.
- [18] C. T. Chantler, "Theoretical form factor, attenuation, and scattering tabulation for  $Z = 1 - 92$  from  $E = 1 - 10$  eV to  $E = 0.4 - 1.0$  MeV," *Journal of Physical and Chemical Reference Data*, vol. 24, no. 1, p. 71, 1995.
- [19] C. T. Chantler, "Detailed tabulation of atomic form factors, photoelectric absorption and scattering cross section, and mass attenuation coefficients in the vicinity of absorption edges in the soft X-ray ( $Z = 30 - 36$ ,  $Z = 60 - 89$ ,  $E = 0.1 - 10$  keV)—addressing convergence issues of earlier work," *Journal of Physical and Chemical Reference Data*, vol. 29, no. 4, p. 597, 2000.

## Research Article

# A Performance Evaluation of a Notebook PC under a High Dose-Rate Gamma Ray Irradiation Test

Jai Wan Cho and Kyung Min Jeong

*Nuclear Convergence Division, Korea Atomic Energy Research Institute, 989-111 Daedeok-Daero, Yuseong-Gu, Daejeon 305-353, Republic of Korea*

Correspondence should be addressed to Jai Wan Cho; [jwcho@kaeri.re.kr](mailto:jwcho@kaeri.re.kr)

Received 13 November 2013; Accepted 4 January 2014; Published 12 February 2014

Academic Editor: Jakrapong Kaewkhao

Copyright © 2014 J. W. Cho and K. M. Jeong. This is an open access article distributed under the Creative Commons Attribution License, which permits unrestricted use, distribution, and reproduction in any medium, provided the original work is properly cited.

We describe the performance of a notebook PC under a high dose-rate gamma ray irradiation test. A notebook PC, which is small and light weight, is generally used as the control unit of a robot system and loaded onto the robot body. Using TEPCO's CAMS (containment atmospheric monitoring system) data, the gamma ray dose rate before and after a hydrogen explosion in reactor units 1–3 of the Fukushima nuclear power plant was more than 150 Gy/h. To use a notebook PC as the control unit of a robot system entering a reactor building to mitigate the severe accident situation of a nuclear power plant, the performance of the notebook PC under such intense gamma-irradiation fields should be evaluated. Under a similar dose-rate (150 Gy/h) gamma ray environment, the performances of different notebook PCs were evaluated. In addition, a simple method for a performance evaluation of a notebook PC under a high dose-rate gamma ray irradiation test is proposed. Three notebook PCs were tested to verify the method proposed in this paper.

## 1. Introduction

After the criticality accident at the JCO uranium refinery in 1999, Japan developed a number of robot systems for emergency response to accidents at nuclear facilities including nuclear power plants [1–4]. In the nuclear robot system for emergency preparedness developed after the JCO criticality accident in 1999, the radiation-hardness design life (20 Gy total irradiation dose) of the robot control unit including electronic circuits, devices, and Toughbook notebook PC was determined assuming that the robot should work for two hours in 10 Gy/h gamma ray dose-rate environments [5]. TEPCO (Tokyo Electric Power Company) improved a Quince robot for responding to underground facility disasters, developed by the Chiba Institute of Technology and Tohoku University, and used it in the accident at the Fukushima Daiichi nuclear power plant [6]. The radiation resistance of the commercial electronic parts used in the Quince robot was evaluated through a gamma ray irradiation experiment using a Co-60 gamma ray source on April 15 and April 20, 2011. A 200 Gy TID (for 10 hours at a 20 Gy/h dose rate) was irradiated onto

the CPU board and camera. The experimental results showed that the camera failed at over a 169 Gy cumulative irradiation dose, while the CPU board worked normally [7]. During the accident at the Fukushima Daiichi nuclear power plant, the gamma ray dose rate before and after the nuclear reactor core meltdown, followed by a hydrogen explosion in units 1 and 3 reactor buildings, was more than 150 Sv/h [8]. The ultimate objective of nuclear power plant safety is to prevent the release of radioactive material into the environment. To achieve this objective, a robot system for emergency preparedness in a nuclear power plant should enter the reactor building and PCV (primary containment vessel) and carry out missions to manipulate vent valve operations for the discharge of radioactive gas through a stack. In the stack, a filtration unit is installed to remove radionuclides so that the release of radioactive material into the atmospheric environment can be prevented. Therefore, assuming that a robot system enters the reactor building to prevent or mitigate a severe accident in a nuclear power plant, the robot system should be able to manipulate the components for supplying water inside the reactor area to cool down the decay heat of the reactor core

and the valves (open or close) for gas (or steam) discharge in a gamma ray dose-rate environment of more than 150 Sv/h. This means that the robot control unit (notebook PC) composed of semiconductor typed electronic devices, which are embedded in the main body of the robot system, can be operated reliably in a high radiation environment of more than a 150 Sv/h gamma ray dose rate.

In this paper, we describe the performance of a notebook PC under a high dose-rate gamma ray irradiation test. Under the 150 Gy/h gamma ray dose-rate irradiation environments, the performances of notebook PCs are evaluated using an online method. In addition, a simple method for a performance evaluation of a notebook PC under high dose-rate gamma ray irradiation test is proposed. The method uses an abrupt change in the speckle distribution owing to gamma ray irradiation. A notebook PC under high dose-rate gamma ray irradiation test is placed at the target distance from the Co-60 (gamma ray) source. A pilot application program for checking the status of the notebook PC under gamma ray irradiation testing is executed on the same notebook PC under test. The menus of the pilot application programs are then displayed on the LCD screen of the PC under test. A CCD (or CMOS) camera is placed relatively far from the gamma ray source, compared to the target distance of the notebook PC under test. By monitoring an LCD screen using a CCD camera, positioned far from the notebook PC under a gamma ray irradiation test, we can observe the status of the pilot application program (i.e., the operation status of the notebook PC). As the monitoring CCD camera is far from the Co-60 gamma ray source compared to the notebook PC under testing, the intensity of the gamma ray, irradiated onto the monitoring CCD camera, is weak. However, speckles from gamma ray irradiation appeared in the monitoring CCD camera image. When there was no change in the background (gamma ray irradiation facility) during the gamma ray irradiation test, the speckle distribution appearing in the monitoring camera image was uniform. A uniform speckle distribution means that the test sample (notebook PC) is exposed to a constant radiation dose rate. As the irradiation time is increased, the cumulative radiation exposure dose in the notebook PC is also increased. The status of the pilot application program changes abruptly when the totally irradiated dose of the notebook PC exceeds the radiation-hardened dose level of the notebook PC. In this case, the menu of the pilot application program disappears from the LCD screen of the notebook PC, or the menu of an unexpected application program appears, thereby causing an abrupt change in the speckle distribution. By detecting this change in the speckle distribution, it is possible to easily discriminate a performance degradation of the notebook PC under a high dose-rate gamma ray irradiation test.

## 2. Gamma Ray Dose Rate before and after Hydrogen Explosion

Owing to the SBO (station blackout, i.e., complete loss of AC power in the power plant) caused by an earthquake and tsunami, reactor units 1–3 at the Fukushima Daiichi nuclear

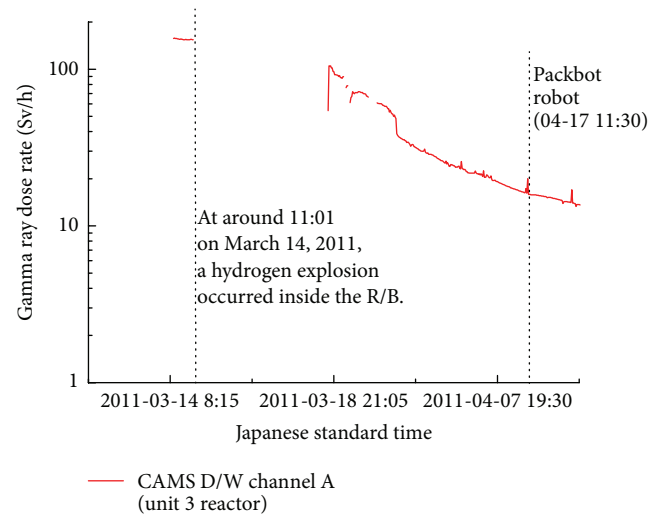


FIGURE 1: Gamma ray dose rates of the PCV D/W area in unit 3 reactor.

power plant lost their emergency core cooling function. In the case of unit 1 reactor, even the instrumentation system did not work owing to the inundation of the DC power source supplied by the backup batteries. According to CAMS (containment atmospheric monitoring system) data of the PCV D/W (dry well) region in unit 1 reactor, which was announced by TEPCO, the gamma ray dose rate was 164 Sv/h on March 14, 06:00, at which time more than one day had passed since the hydrogen explosion on March 12, 15:36. In the case of unit 2 reactor, the maximum dose rate was 138 Sv/h in the CAMS D/W channel at the time of the meltdown, which was followed by PCV damage. In the case of unit 3 reactor, the maximum dose rate was 167 Sv/h before the hydrogen explosion (March 14, 11:01) and 154 Sv/h after it. Figure 1 shows the gamma ray dose-rate distribution of the PCV D/W region of unit 3 reactor. The  $x$ -axis in Figure 1 represents about one month of measurement time, from before the hydrogen explosion to when the Packbot robot entered unit 3 reactor building for the first time (April 17, 11:30). The measurement time interval was one hour, on average. The  $y$ -axis represents the gamma ray dose rate. Unit 3 reactor experienced a hydrogen explosion around March 14, 2011, at 11:01, and the gamma ray dose rate in CAMS D/W channel A at the time immediately before the explosion (March 14, 10:55) was 154 Sv/h. No measurement data were provided for more than four days, owing to the impact of the hydrogen explosion. In addition, the gamma ray dose rate in CAMS D/W channel A at the time of the Packbot robot entry was 15.9 Sv/h.

Figure 1 shows the gamma ray dose-rate distribution in the atmosphere between the exterior wall of the RPV (reactor pressure vessel) and the inner wall of the PCV. Since the Packbot robot system entered an area between the exterior wall of the PCV and the inner wall of the reactor building (R/B), it carried out its mission in a much lower dose-rate environment than that of the measured value in the CAMS D/W channel.

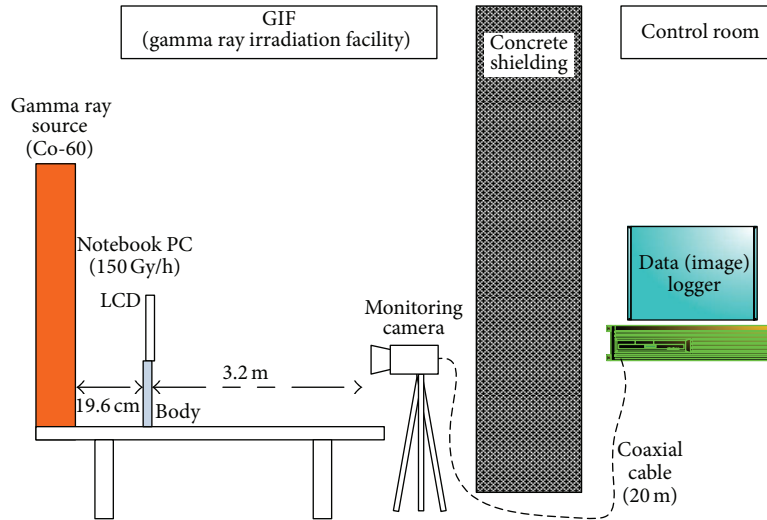


FIGURE 2: Schematic diagram for gamma ray irradiation test of the notebook PC.

### 3. Experiments

Figures 2 and 3 show the experimental setup. The notebook PC under test was gamma ray irradiated at a dose rate of 150 Gy/h (19.6 cm distance from Co-60 gamma ray source) until failure. A pilot application program to check the abnormal status of the notebook PC owing to the cumulative gamma ray irradiation dose was executed. A RS-232C loopback test program was executed as the pilot application program, and the menu of the pilot application program was displayed on the LCD screen of the notebook PC under the gamma ray irradiation test. Then, using another monitoring CCD camera, installed at a 340 cm distance (2.11 Gy/h) from the radiation source (Co-60), the LCD screen of the notebook PC under test was observed online. We adjusted the field of view of the monitoring CCD camera such that the LCD screen of the notebook PC under gamma ray irradiation testing was shown fully on the image plane of the monitoring CCD camera. The distance of the monitoring CCD camera from the Co-60 source was determined to be relatively long compared to the notebook PC under test because the camera should robustly observe the status of the pilot application program until the notebook PC under the gamma ray irradiation test failed. As shown in Figures 2 and 3, the main body of the notebook PC under test is nearer to the Co-60 gamma ray source than the LCD screen of the notebook PC under test. Thus, the intensity of the gamma ray dose-rate irradiated at the main body of the notebook PC under test is greater than the LCD screen of the same notebook PC under test. Assuming that the ASIC FPGA, CPU, DSP, and electronic devices, which are generally used in the LCD driver unit and main body of the notebook PC, are made through the CMOS fabrication process, we can estimate that the main body of the notebook PC will fail to function prior to the LCD screen of the same PC as the gamma ray irradiation time elapsed. To discriminate an accurate malfunction point of the notebook PC under a gamma ray irradiation test, the time log is marked on the upper position of the image plane of the monitoring camera. In addition, the observation image of the LCD screen

of the notebook PC under testing was periodically recorded on the hard disk of the data logger system (notebook PC), placed in the control room as shown in Figure 2. A USB-2-RS232C conversion module for the RS-232C loopback test is placed behind the lead block (50 × 100 × 200 mm), as shown in Figure 3. As the thickness of the lead block is 50 mm, the intensity of the gamma ray dose-rate irradiated at the USB-2-RS232C conversion module is reduced by less than 1/10. The TVT (tenth value thickness) of the lead material for the Co-60 gamma ray source is 40 mm [9]. The TVT is the thickness of material required to reduce the gamma radiation to one-tenth the intensity. As the cumulative gamma ray irradiation dose increases, the status of the pilot application program of the notebook PC under gamma ray irradiation test is estimated to change. When the notebook PC is under a normal status, the menu screen of the pilot application program does not change. Therefore, speckles appearing in the image of the monitoring CCD camera show a uniform distribution. When the notebook PC is over irradiated beyond the endurance limit of the cumulative gamma ray dose, a subtle change in the menu screen of the pilot application program of the notebook PC under test occurs. By detecting this, the abnormality of the notebook PC owing to a cumulative gamma ray dose beyond the endurance limit can be identified.

### 4. Results and Discussion

Figure 4 shows the menu screen of the pilot application program executed in the notebook PC under test before the gamma ray irradiation. Figure 5 shows the menu screen of the pilot application program (RS-232C loopback test) of the notebook PC under test during the gamma ray irradiation. The unique difference between Figures 4 and 5 is the speckles. Before the gamma ray source (Co-60) is placed at its irradiation point, the menu of the pilot application program is only observed in the monitoring CCD camera image, as shown in Figure 4. After the source is uploaded to its irradiation position, speckles from the gamma ray are

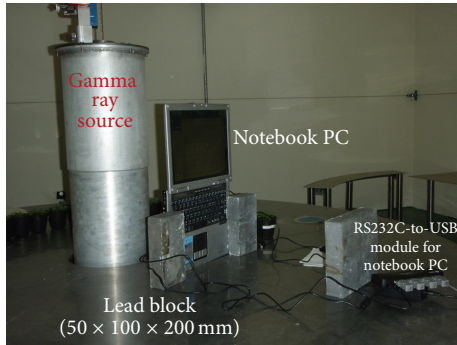


FIGURE 3: Experimental setup for the notebook PC under a high dose-rate gamma ray irradiation test.

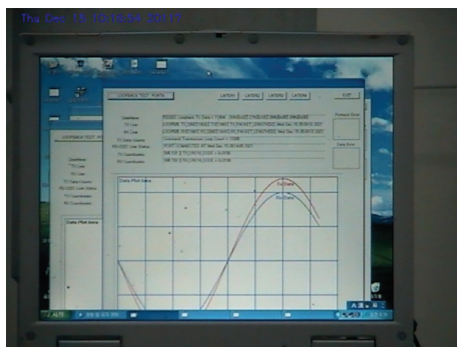


FIGURE 4: Menu image of the pilot application program, executed on a notebook PC under test (before gamma ray irradiation).

superimposed onto the image of the monitoring camera, as shown in Figure 5. In Figure 5, the white dots in the yellow circles are speckles.

Figure 6 shows the failure of the pilot application program observed at a time when the cumulative gamma ray irradiation dose of the notebook PC under test was about 225 Gy ( $150 \text{ Gy/h} \times 1.5 \text{ h}$ ). Figure 6(a) shows the menu of the pilot application program when the notebook PC under test is in a normal state during the high dose-rate gamma ray irradiation. In Figure 6(a), the red (TX) and blue (RX) curves shown in the menu of the pilot application program (RS-232C loopback test) of the notebook PC under test represent the status of the data transmission experiment during the high dose-rate gamma ray irradiation test. If a data transmission error occurs, the peak is drawn in the received waveform (blue curve) at the time of error occurrence, as shown in Figure 6(a). This means that the notebook PC under a high dose-rate gamma ray irradiation test is operating normally. Figures 6(b) and 6(c) show images immediately before and after the malfunction of the notebook PC under test. After approximately 81 minutes elapsed, the LCD screen of the notebook PC under test was abruptly changed. As shown in Figures 6(c) and 6(d), the LCD screen of the notebook PC under test blacked out.

To discriminate whether the failure (phenomena of the LCD screen blackout) of the notebook PC under test was caused by the LCD driver unit or the main body of the same



FIGURE 5: Menu image of the pilot application program, executed on a notebook PC under test (during gamma ray irradiation, about 15 min elapsed).

PC, an extended test of the postirradiated notebook PC was conducted for 24 hours in a laboratory (room temperature environment) similar to a control room environment after the gamma ray irradiation experiment was over. Thus, test programs were executed again for 24 hours in the postirradiated notebook PC. In this test, we continuously monitored the LCD screen of the postirradiated notebook PC. Until the initial 4 hours approximately, the notebook PC was normally operated as shown in Figure 7(a). After that, there were abrupt changes in the menu screen of the initial setup of the postirradiated notebook PC (shown in Figure 7(b)), and the windows of various unintended application programs appeared and disappeared repetitively from the LCD screen of the notebook PC, as shown in Figures 7(b), 7(c), and 7(d). From such observation, we could convince that there was no problem in the LCD driver unit and some functions related with LCD display were not working properly in the main body of the notebook PC during the gamma ray irradiation test.

Gamma ray energy is emitted through a nuclear decay reaction of Co-60. If a CCD camera is exposed to a high-energy gamma ray, white noises (speckles) are generated in the CCD camera image sensor. Since the decay of the Co-60 gamma ray source occurs randomly, speckles in the image of the CCD camera, exposed by the high-energy gamma ray source, appeared randomly frame by frame. It can be assumed that the pixel positions of the speckles in the image plane of the CCD camera, generated from the gamma ray irradiation, are also different frame by frame. Although the speckle distribution shown in the two-dimensional CCD image sensor plane is similar, the speckles appearing at certain pixel coordinates of the current image frame of the CCD camera are hardly generated at the same pixel coordinates of the next image frame of the CCD camera. The half-life of the Co-60 radiation source is approximately more than five years. A characteristic of gamma ray energy emitted from the Co-60 source does not change during an approximately two-hour irradiation period. Therefore, we can calculate the number of speckles in the image plane of the monitoring CCD camera, generated from gamma ray irradiation. Speckles from gamma rays are shown well in Figures 6(c) and 6(d). In this paper, the number of speckles generated from gamma rays was

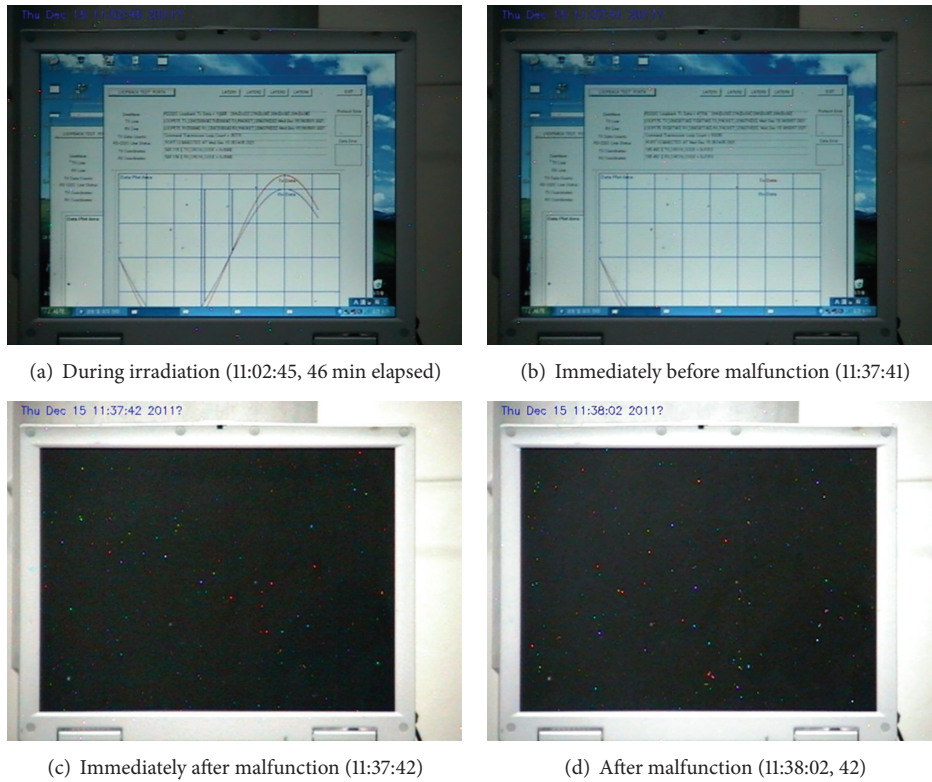


FIGURE 6: Menu images of the pilot application program, executed on a notebook PC under a high dose-rate gamma ray irradiation test.

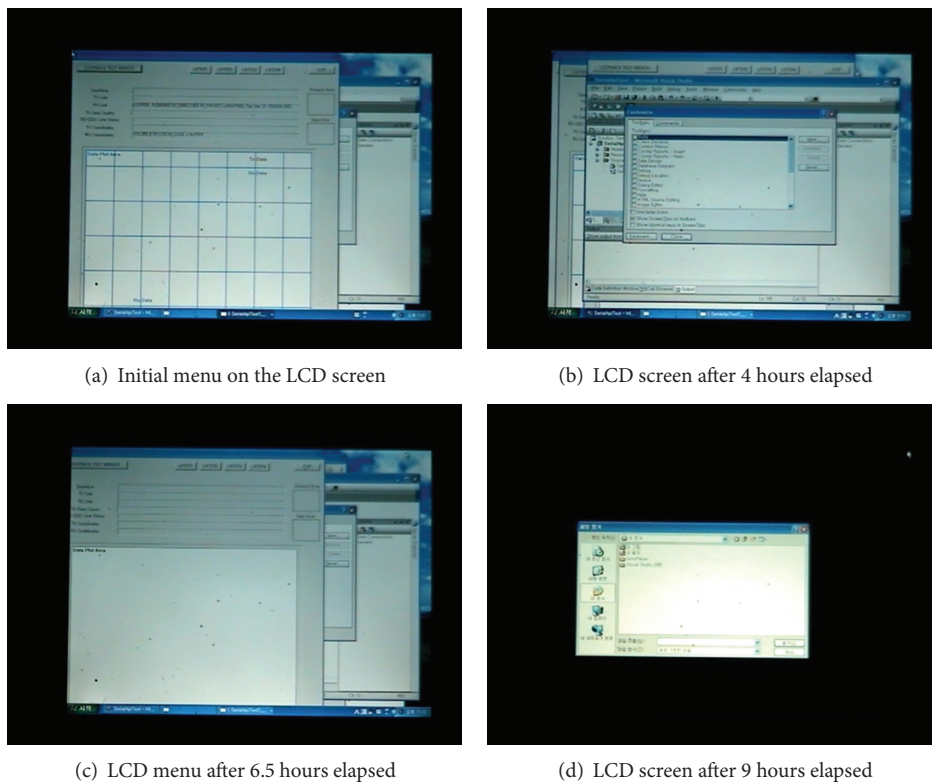


FIGURE 7: LCD screen changes of the postirradiated notebook PC during the annealing test after gamma ray irradiation experiment.

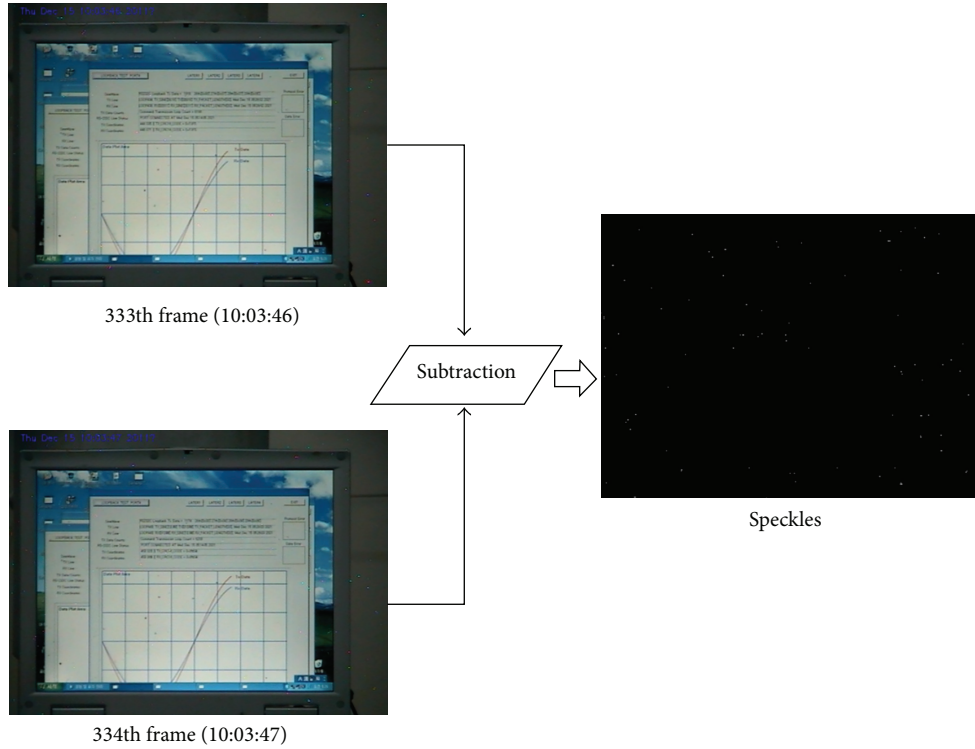


FIGURE 8: Speckle extraction using an image subtraction algorithm.

calculated through an image processing technique. Since the notebook PC under the gamma ray irradiation test and the monitoring CCD camera were placed at a fixed position in the gamma ray irradiation facility and the surrounding environments (background) are not changed, speckle components generated from the gamma rays can be extracted simply using a background subtraction method. The number of speckles is calculated by (1) and (2):

$$\Delta I_n = I_n - I_{n-1}, \quad (1)$$

where  $\Delta I_n$  is a differential image and  $I_n$  and  $I_{n-1}$  are the  $n$ th and  $n-1$ th image frame, respectively. The number of speckles is extracted using the image subtraction algorithm of the previous ( $n-1$ )th image frame from the current ( $n$ )th image frame.  $G_{i,j}$  is a gray level at the  $(i, j)$  position in the differential image  $\Delta I_n$ . And  $G_{\text{threshold}}$  is a threshold value to remove noises in the  $\Delta I_n$  image.  $S_{i,j}$  is a speckle at the  $(i, j)$  coordinates in the differential image  $\Delta I_n$ . Consider

$$\Delta I_n \text{ Speckles total counts} = \sum_{i=1}^n \sum_{j=1}^m S_{ij}, \quad (2)$$

$$S_{ij} = 1, \quad \text{if } G_{ij} \geq G_{\text{threshold}},$$

$$S_{ij} = 0, \quad \text{else } G_{ij} < G_{\text{threshold}}.$$

Figure 8 shows the speckle extraction procedure using (1) and (2). As shown in Figure 8, speckles in the graphed region of the pilot application program are hidden by the white component of the drawing area.

Figure 9 shows the speckle distribution calculated from the images of the monitoring CCD camera, which observed

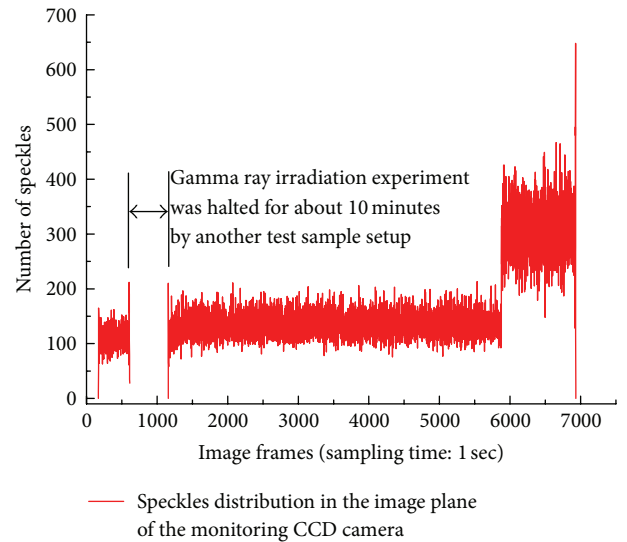


FIGURE 9: Speckles distribution of the CCD monitoring camera images.

and recorded the LCD screen of the notebook PC under the high dose-rate gamma ray irradiation test.

In Figure 9, the numbers in the  $x$ -axis represent the numbers of image frames, stored at one-second intervals during the gamma ray irradiation period; that is, the  $x$ -axis is the irradiation time (frame numbers  $\times$  sampling time). The  $y$ -axis shows the number of speckles calculated using (1) and (2). In Figure 9, the number of speckles up to approximately the 5,878th frame was around 130 on average; the number of speckles after that frame was around 300. From this result,

it can be seen that the reliable performance of the notebook PC under a high dose-rate gamma ray irradiation test was degraded after the 5,878th frame, which was the time when a change in the speckle distribution occurred abruptly from the normal status, as shown in Figure 6(b), to an abnormal (blackout of menu screen) status, as shown in Figure 6(c). Since the menu screen of the pilot application program of the notebook PC under gamma ray irradiation test had a white background, as shown in Figures 6(a) and 6(b), speckles (white components) generated by the gamma rays were not unveiled well under the condition of the bright white background. The reason for the subsequent high distribution of speckles after the 5,878th frame was because the FOV background of the monitoring CCD camera was changed owing to the blackout of the menu screen of the pilot application program of the notebook PC under the gamma ray irradiation test. Since the background screen of the application program for the online test of the notebook PC was white before failure, speckles (white components) generated in the image of the monitoring CCD camera from the gamma rays were veiled in the bright white background screen and therefore showed a small distribution. Then, after failure of the notebook PC, the menu screen of the pilot application program was blacked out, and the background screen was darkened; speckles (white components) generated in the image of the monitoring CCD camera due to the gamma rays were well unveiled in the dark background screen and thereby showed a relatively high distribution. The limiting conditions (cumulative irradiation dose) for normal operation of the notebook PC under high dose-rate (150 Gy/h) gamma ray environments can be obtained, assuming that the image frame number that showed abrupt changes in the speckle distribution was 5,878, as shown below:

$$\text{TID}_{\text{dose limit of notebook PC}} = \frac{(612 - 166) + (5,878 - 1,157)}{3,600} \text{ (h)} \quad (3)$$

$$\times 150 \text{ (Gy/h)} \cong 215 \text{ Gy.}$$

In (3), 612 is the image frame number when the Co-60 source returns to its shelter, and 166 is the image frame number of the monitoring camera when the gamma ray irradiation experiment starts. The time span for first gamma ray irradiation experiment is 446 seconds. And the elapsed time for 2nd gamma ray irradiation experiment is about 1.3 hours. Table 1 shows comparisons of the notebook PCs under high dose-rate gamma ray irradiation testing.

In the case of the 2nd sample, although the menu of the pilot application program disappeared from the LCD screen of the notebook PC under testing, the core function of the pilot application program worked normally for 134 minutes until the cumulative gamma ray irradiation dose reached 337 Gy (150 Gy/h  $\times$  134 min/60 min). The notebook PC (3rd sample) under a high dose-rate gamma ray irradiation testing survived for 110 minutes. After 94 minutes had elapsed, the menu of the pilot application program (image acquisition program) disappeared by an unexpected interruption. It is estimated that the memory (DRAM) module of the notebook

TABLE 1: Performance evaluation results of the notebook PCs under high dose-rate gamma ray irradiation test.

Test samples (notebook PC)	Dose rate (Gy/h)	Pilot application program	TID at simple failure* <sup>1</sup>	TID at irrecoverable failure* <sup>2</sup>
1 (IWORKS)	150	RS-232C loopback test program	215 Gy	312 Gy
2 (SENS P30)	150	Image acquisition program	247 Gy	337 Gy
3 (X NOTE)	150	Image acquisition program	235 Gy	275 Gy

\*<sup>1</sup>The menu of the pilot application program disappeared from the LCD screen of the notebook PC under test, but the core function of the pilot application program had been normally operated until the irrecoverable dose; \*<sup>2</sup>the startup of the notebook PC was unavailable after irrecoverable dose.

PC malfunctioned from an overdose of gamma rays. Thus, 94 minutes is considered a robust operation time when assuming that the notebook PC (3rd sample) would be used as the control unit of a robot system.

## 5. Conclusions

In this paper, a method for detecting an abnormal status of notebook PCs, resulting from a cumulative gamma ray irradiation dose, was proposed. The method uses the transient of a speckle distribution appearing in the CCD image owing to the gamma ray irradiation. A notebook PC (test sample) under a gamma ray irradiation survivability test is placed at a certain distance from the gamma ray source. A CCD camera for monitoring the status of the notebook PC under testing is placed at a relatively farther distance, compared to the notebook PC, from the gamma ray source. Then, a pilot application program is executed on the notebook PC under a high dose-rate gamma ray test. A menu of the pilot application program is displayed on the LCD screen of the notebook PC under test. The CCD camera observes the LCD screen of the notebook PC under test. In the monitoring image of the CCD camera, the menu of the pilot application program is viewed including speckles. Speckles appearing in the CCD camera image show that the notebook PC under test is normally gamma ray irradiated. When the notebook PC is overirradiated beyond the endurance limit of the cumulative gamma ray dose, a transient in the menu screen of the pilot application program, executed on the notebook PC under test, occurred. By detecting this using a CCD camera, the abnormality of the notebook PC owing to a cumulative gamma ray irradiation dose beyond the survivability limit could be identified.

In this paper, to calculate the speckle distribution generated in the observation camera from a gamma ray, the background subtraction processing technique was used. The gamma ray dose rate for the notebook PC under test

was set at 150 Gy/h by considering the gamma ray dose rate, measured before the hydrogen explosion that occurred in units 1 and 3 reactor buildings of the Fukushima Daiichi nuclear power plant. As the irradiation time increased and the cumulative irradiation dose of the notebook PC under test exceeded the threshold, a transient operation in the menu of the pilot application program, executed on the notebook PC under test, was found. The menu of the pilot application program disappeared, or the menu of the nondemanded application programs appeared on the LCD screen of the notebook PC under test, thereby making changes in the speckle distribution. By detecting this change in speckle distribution, the degradation time from the cumulative gamma ray irradiation dose of the notebook PC under test can be estimated accurately. The experimental results verified that the notebook PC, which can be used as a control unit of a robot controller, operated robustly without malfunctions for about 90 minutes under the 150 Gy/h gamma ray dose-rate environments.

### Conflict of Interests

The authors declare that there is no conflict of interests regarding the publication of this paper.

### Acknowledgments

This work was supported by the National Research Foundation of Korea (NRF) grant funded by the Korean government (MSIP) (NRF-2012M2A8A1029350 and NRF-2012M2A8A5025657).

### References

- [1] T. Mano and S. Hamada, "Development of robotic system for nuclear facility emergency preparedness," *Journal of the Robotics Society of Japan*, vol. 19, no. 6, pp. 714–721, 2001 (Japanese).
- [2] T. Kobayashi, K. Miyajima, and S. Yanagihara, "Development of robots for nuclear accidents in Japan atomic energy research institute—1: development of remote surveillance squad," *Journal of the Robotics Society of Japan*, vol. 19, no. 6, pp. 706–709, 2001 (Japanese).
- [3] K. Shibanuma, "Development of rescue robot at JAERI. Part 2: development of radiation-proof robot," *Journal of the Robotics Society of Japan*, vol. 19, no. 6, pp. 710–713, 2001 (Japanese).
- [4] J. Nakayama and M. Sugimoto, "Information gathering robots for nuclear accidents," *Research and Development Kobe Steel Engineering Reports*, vol. 53, no. 3, pp. 89–91, 2003 (Japanese).
- [5] Disaster Response Robotics Task Force, "Radiation Hardness Evaluation of the Parts for the General Purpose Heavy Machines and Robotics (Japanese)," 2011, <http://roboticstaskforce.wordpress.com/>.
- [6] K. Nagatani, S. Kiribayashi, Y. Okada et al., "Redesign of rescue mobile robot Quince—toward emergency response to the nuclear accident at Fukushima Daiichi Nuclear Power Station on March 2011," in *Proceedings of the 9th IEEE International Symposium on Safety, Security, and Rescue Robotics (SSRR '11)*, pp. 13–18, Kyoto, Japan, November 2011.
- [7] K. Nagatani, S. Kiribayashi, Y. Okada et al., "Gamma-ray irradiation test of electric components of rescue mobile robot Quince—toward emergency response to nuclear accident at Fukushima Daiichi Nuclear Power Station on March 2011," in *Proceedings of the 9th IEEE International Symposium on Safety, Security, and Rescue Robotics (SSRR '11)*, pp. 56–60, Kyoto, Japan, November 2011.
- [8] TEPCO, "Fukushima Daiichi Nuclear Power Station Unit 1~3, Parameters of Water level, Pressure, CAMS, and etc.," 2012, <http://www.tepco.co.jp/nu/fukushima-np/fl/pla/index-j.html>.
- [9] Environmental Health and Safety, University of Toronto, "Module 7: radiation safety," <http://www.ehs.utoronto.ca/services/radiation/radtraining/module7.htm>.

## Research Article

# The Application of Microdosimetric Principles to Radiation Hardness Testing

**Jeremy D. Northum and Stephen B. Guetersloh**

*Department of Nuclear Engineering, Texas A&M University, MS 3133, College Station, TX 77840, USA*

Correspondence should be addressed to Jeremy D. Northum; [jnorthum@tamu.edu](mailto:jnorthum@tamu.edu)

Received 10 October 2013; Accepted 22 November 2013; Published 12 January 2014

Academic Editor: Jakrapong Kaewkhao

Copyright © 2014 J. D. Northum and S. B. Guetersloh. This is an open access article distributed under the Creative Commons Attribution License, which permits unrestricted use, distribution, and reproduction in any medium, provided the original work is properly cited.

Chord length distributions for rectangular parallelepipeds of various relative dimensions were studied in relation to radiation hardness testing. For each geometry, a differential chord length distribution was generated using a Monte Carlo method to simulate exposure to an isotropic radiation source. The frequency and dose distributions of chord length crossings for each geometry, as well as the means of these distributions, are presented. In every case, the dose mean chord length was greater than the frequency mean chord length with a 34.5% increase found for the least extreme case of a cube. This large increase of the dose mean chord length relative to the frequency mean chord length demonstrates the need to consider rare, long-chord-length crossings in radiation hardness testing of electronic components.

## 1. Introduction

Microdosimetry is the study of the patterns of energy deposition from ionizing radiation interacting with microscopic volumes much smaller than the range of secondary particles generated by the incident particle. Since its inception less than 50 years ago, it has been very important in the field of radiobiology [1]. Because of this, metrics evolved around a standard geometry of a  $1\ \mu\text{m}$  sphere [2] and published results from experimental measurements are related to radiation interaction with a spherical or cylindrical detector. Over the past decade or so, increasingly small components have been developed to meet the demands of the electronics industry and, as a result, the amount of charge necessary for inducing a single event effect (SEE) becomes correspondingly smaller [3]. In deep space SEE production results mainly from the traversal by heavy ions that make up the galactic cosmic ray (GCR) spectrum. In low-Earth orbits SEE production is dominated by proton-induced spallation reactions [3]. As many of the components manufactured today can easily have dimensions on the order of several micrometers, the principles of microdosimetry have application in stability testing of these microchips intended for use in radiation

fields. However, the differences in geometry between the sphere and the parallelepiped need to be considered.

A significant amount of work has been performed at accelerator facilities to test the radiation hardness of electronic components. Attention is often given to the influence of geometric factors on SEE rates. While several recent studies have considered the incident angle of the beam in radiation hardness testing [4–7], many apparently do not [8, 9] and this is a crucial factor when analyzing upsets as a function of energy delivered. It is recognized that some radiation hardness testing has been focused on the influence of beam energy, linear energy transfer (LET), and other nongeometry factors or has had geometry factors as a secondary area of study.

Even with that recognition in mind, it seems as though insufficient consideration has been given to geometric effects, specifically, the influence of long-chord-length crossings on the dose to the component of interest. It will be demonstrated, through an analysis of chord length distributions, that these long-chord-length crossings, despite their relative infrequent occurrence, are too important to be ignored and must be considered to completely assess an electronic component's susceptibility to SEEs.

Studying the chord length distributions produced by random traversals relating to radiation hardness testing is not a novel concept. Previous work has considered both the differential [10–12] and integral [11] chord length distributions. What is unique, however, is the present consideration of the dose distributions for chord length crossings in addition to the commonly used frequency distribution.

## 2. Methods

The original driving force in the evolution into modern microdosimetry was the need to characterize the LET of the incident radiation as it is used somewhat as a marker of the radiation's damaging ability [1]. LET, commonly used in radiation hardness testing of microelectronics, is a macroscopic average of the energy lost by the incident radiation in the direction of traversal and classically carries units of MeV/cm [13]. For use in radiation biology and due to the size of the target studied, these units were seen as less than sufficient so a factor of 10 is employed converting LET into units of keV/ $\mu\text{m}$ , where  $10 \text{ MeV/cm} = 1 \text{ keV}/\mu\text{m}$ , now much more meaningful to the volumes of concern. This, however, does not solve the problem that LET is a one-dimensional concept that does not describe the radial extent of energy transfer [14, 15]. At the macroscopic level, different incident particles may have the same LET at some point along their path but, due to the dependence of secondary delta-ray energy as a function of velocity, the local energy deposited may be very different due to energy escaping the volume of interest. This radial energy loss is a factor of both the incident ion velocity and the target geometry. Therefore, microscopic energy measurements are commonly presented in terms of the stochastic energy deposition or dose distributions in the volume and geometry relevant to the study [3].

The most common stochastic value used in microdosimetry measurements and simulations is lineal energy. The lineal energy  $y$  is

$$y = \frac{\epsilon}{\bar{l}}, \quad (1)$$

where  $\epsilon$  is the energy imparted to the matter in a given volume by a single energy-deposition event and  $\bar{l}$  is the mean chord length of the volume [3]. The mean chord length of a convex body is

$$\bar{l} = \frac{4V}{S}, \quad (2)$$

where  $V$  is the volume and  $S$  is the surface area [16].

Microdosimetry spectra [3] are commonly expressed in terms of the lineal energy  $y$ , its differential distribution  $f(y)$ , and the mean of this distribution  $\bar{y}_F$  which is

$$\bar{y}_F = \int_0^{\infty} y f(y) dy. \quad (3)$$

The dose distribution, reflecting the fact that higher lineal energies deposit a higher dose [17], is also often considered where

$$d(y) = \frac{y f(y)}{\bar{y}_F} \quad (4)$$

and the mean of this distribution, the dose mean lineal energy, is

$$\bar{y}_D = \frac{1}{\bar{y}_F} \int_0^{\infty} y^2 f(y) dy, \quad (5)$$

where  $\bar{y}_F$  is the frequency mean lineal energy from (3). The frequency mean lineal energy  $\bar{y}_F$  is the first moment of the  $f(y)$  distribution and the dose mean lineal energy  $\bar{y}_D$  is the ratio of the second and first moments of the  $f(y)$  distribution [3].

For the case of radiation hardness testing, the methodology of  $y$  can be applied to the chord length of a convex body. Thus, the frequency distribution of the chord length  $f(l)$  has a mean value of

$$\bar{l}_F = \int_0^{\infty} l f(l) dl, \quad (6)$$

where  $l$  is the differential chord length. The frequency mean chord length  $\bar{l}_F$  calculated by (6) is the numerical equivalent to the analytical value  $\bar{l}$  calculated by (2). It must be kept in mind that this value is the frequency mean chord length and this equivalence between  $\bar{l}_F$  and  $\bar{l}$  only exists because of the isotropic nature of space radiation. This equivalence does not exist for nonisotropic sources.

Likewise, again applying the fact that longer chord lengths result in a higher energy imparted [17], the dose distribution is

$$d(l) = \frac{l f(l)}{\bar{l}_F} \quad (7)$$

with a mean value of

$$\bar{l}_D = \frac{1}{\bar{l}_F} \int_0^{\infty} l^2 f(l) dl, \quad (8)$$

where, again,  $l$  is the differential chord length. These chord length mean values have the same relationship to the  $f(l)$  distribution as the  $y$  mean values did to the  $f(y)$  distribution. The frequency mean chord length  $\bar{l}_F$  is the first moment of the  $f(l)$  distribution and the dose mean chord length  $\bar{l}_D$  is the ratio of the second and first moments of the  $f(l)$  distribution.

The value  $\bar{l}_D$  is the dose mean chord length, that is, the chord length equal to the mean of the  $d(l)$  distribution. It is these frequency and dose mean chord lengths, and perhaps more importantly the difference between the two, that are of interest in radiation hardness testing. As will be seen in the next section, these long-chord-length crossings contribute significantly to the total dose despite their relative infrequency.

A simple Monte Carlo algorithm, based on previous work [18] and utilizing a linear congruential random number generator [19], was implemented to produce the chord length frequency distributions for each geometry. These chord length distributions are equivalent to the path length distributions that would result from exposure to an isotropic source of charged particles. The novelty of this methodology

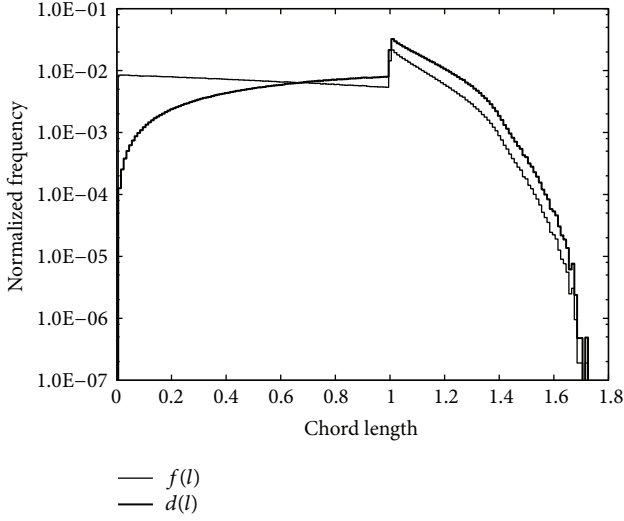


FIGURE 1:  $f(l)$  and  $d(l)$  distributions for a rectangular parallelepiped with relative dimensions  $1 \times 1 \times 1$ .

is contained within the analysis of the chord length distributions; any Monte Carlo algorithm that is capable of generating frequency distributions of chord length will suffice.

Starting with the code-produced frequency distribution  $f(l)$ , the frequency mean chord length  $\bar{l}_F$  was calculated according to (6), the dose distribution  $d(l)$  was produced according to (7), and the dose mean chord length  $\bar{l}_D$  was calculated according to (8). This work is limited in scope to the rectangular parallelepiped (RPP) but the method is applicable to all convex bodies.

### 3. Results and Discussion

Frequency and dose distributions of chord length crossings for RPPs of four unique relative dimensions are presented. In each plot, the normal-line-weight curve represents the frequency distribution  $f(l)$  and the heavy-line-weight curve represents the dose distribution  $d(l)$ .

Figure 1 shows the  $f(l)$  and  $d(l)$  distributions for a RPP with relative dimensions  $1 \times 1 \times 1$ , a cube. The peak at 1.0 corresponds to the dimension of the same value. Figures 2, 3, and 4 show the  $f(l)$  and  $d(l)$  distributions for a noncubic RPP with relative dimensions  $2.5 \times 1 \times 0.625$ ,  $2 \times 2 \times 0.5$ , and  $4 \times 4 \times 0.4$ , respectively. Likewise, the peaks in these distributions correspond to the dimensions of the same value. Each frequency distribution was produced by  $1 \times 10^7$  iterations of the Monte Carlo algorithm [18]. A comparison of  $\bar{l}_F$  and  $\bar{l}_D$  values for each geometry appears in Table 1 along with the percent differences between the two.

Each unique geometry presented has the same  $\bar{l}_F$  value despite having unique  $f(l)$  distributions. In each case, the  $f(l)$  distribution was weighted by  $l$  to produce  $d(l)$ , as described in (7). It is these differences in the  $f(l)$  distributions, as well as the  $l$  weighting found in the  $d(l)$  distributions, that lead to the significant differences in the  $\bar{l}_D$  values despite each geometry having the same  $\bar{l}_F$  value.

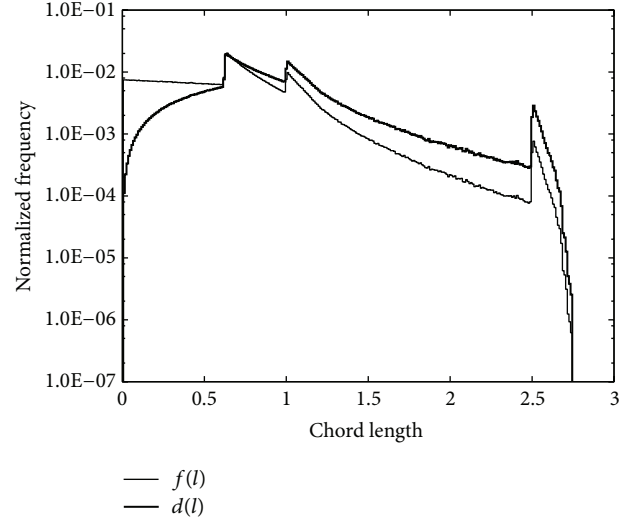


FIGURE 2:  $f(l)$  and  $d(l)$  distributions for a rectangular parallelepiped with relative dimensions  $2.5 \times 1 \times 0.625$ .

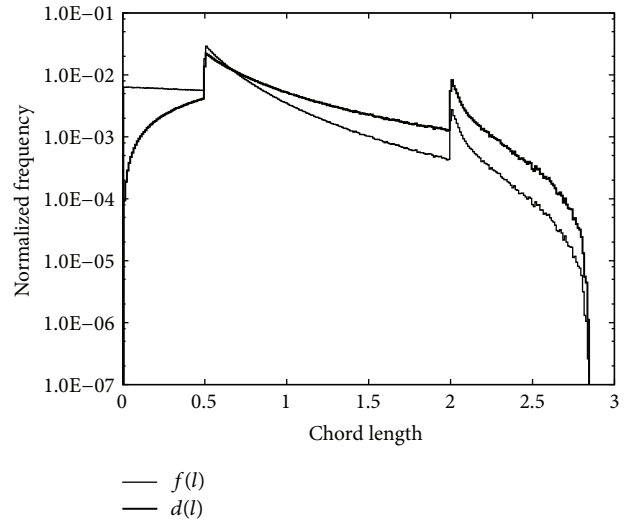


FIGURE 3:  $f(l)$  and  $d(l)$  distributions for a rectangular parallelepiped with relative dimensions  $2 \times 2 \times 0.5$ .

TABLE 1:  $\bar{l}_F$  and  $\bar{l}_D$  values for a selection of rectangular parallelepipeds of varying relative dimensions.

Relative dimensions	$\bar{l}_F$	$\bar{l}_D$	% difference
$1 \times 1 \times 1$	0.667	0.897	34.5
$2.5 \times 1 \times 0.625$	0.667	0.926	38.9
$2 \times 2 \times 0.5$	0.667	0.964	44.6
$4 \times 4 \times 0.4$	0.667	1.10	65.5

While the long-chord-length crossings are quite rare, they represent a disproportionately high contribution to the total dose. This characteristic is made evident by large differences between the  $\bar{l}_F$  and  $\bar{l}_D$  values for each geometry presented in Table 1. Even for the least extreme case of the cube,  $\bar{l}_F$  and  $\bar{l}_D$  differ by 34.5%. As the RPP becomes less cubic, the difference

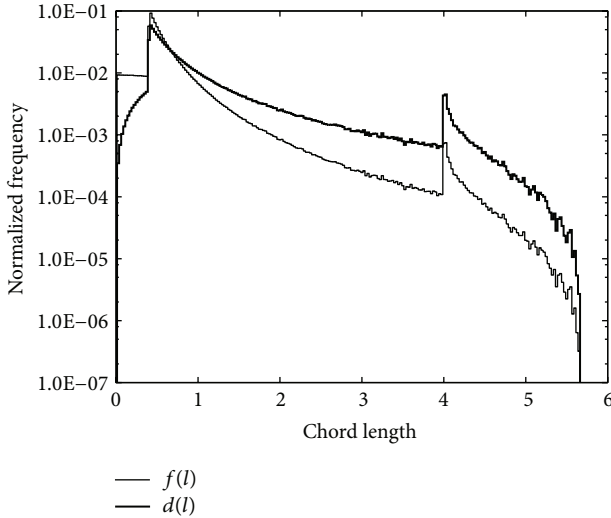


FIGURE 4:  $f(l)$  and  $d(l)$  distributions for a rectangular parallelepiped with relative dimensions  $4 \times 4 \times 0.4$ .

between  $\bar{l}_F$  and  $\bar{l}_D$  increases. For the most extreme case of the RPP with relative dimensions  $4 \times 4 \times 0.4$ ,  $\bar{l}_F$  and  $\bar{l}_D$  differ by 65.5%.

A quick comparison to previous work confirms the validity of the dose mean chord length methodology presented in (8). Since  $\bar{l}_D$  is the ratio of the second and first moments of the  $f(l)$  distribution, it would be expected that the product of  $\bar{l}_F$  and  $\bar{l}_D$  would be equal to the second moment of the  $f(l)$  distribution. Simple arithmetic applied to the RPP of relative dimensions  $1 \times 1 \times 1$ , a unit cube, gives the second moment of the  $f(l)$  distribution as

$$\bar{l}_F \times \bar{l}_D = 0.667 \times 0.897 = 0.598 \quad (9)$$

which matches the value of 0.5978 given by Coleman as the second moment of the distribution of the random path lengths through a unit cube [20].

#### 4. Conclusion

Frequency and dose distributions of chord length crossings were presented for RPPs of varying relative dimensions, each with the same frequency mean chord length. The frequency mean chord length  $\bar{l}_F$  and dose mean chord length  $\bar{l}_D$  were presented for each unique geometry. In every case,  $\bar{l}_D$  was greater than  $\bar{l}_F$ . Even for the least extreme case of the cube,  $\bar{l}_F$  and  $\bar{l}_D$  differ by more than 30%. The significant differences presented between  $\bar{l}_F$  and  $\bar{l}_D$  illustrate the importance of considering long-chord-length crossings in radiation hardness testing despite their relatively low probability of occurrence.

#### Conflict of Interests

The authors declare that there is no conflict of interests regarding the publication of this paper.

#### Acknowledgments

This work was supported by the U.S. Nuclear Regulatory Commission, Faculty Development Program, Grant no. NRC-38-10-923, Contract no. CII-00494. The authors would like to thank Z. Kulage for help with troubleshooting the code.

#### References

- [1] A. M. Kellerer, "Microdosimetry: reflections on Harald Rossi," *Radiation Protection Dosimetry*, vol. 99, no. 1-4, pp. 17-22, 2002.
- [2] J. Booz, L. Braby, J. Coyne et al., "Microdosimetry," Tech. Rep. 36, International Commission on Radiation Units and Measurements, Bethesda, MD, USA, 1983.
- [3] H. H. Rossi and M. Zaider, *Microdosimetry and Its Applications*, Springer, New York, NY, USA, 1996.
- [4] K. P. Rodbell, D. F. Heidel, H. H. K. Tang, M. S. Gordon, P. Oldiges, and C. L. Murray, "Low-energy proton-induced single-event-upsets in 65 nm node, silicon-on-insulator, latches and memory cells," *IEEE Transactions on Nuclear Science*, vol. 54, no. 6, pp. 2474-2479, 2007.
- [5] J. A. Pellish, M. A. Xapsos, K. A. Label et al., "Heavy ion testing at the galactic cosmic ray energy peak," in *Proceedings of the 10th European Conference on Radiation and Its Effects on Components and Systems (RADECS '09)*, pp. 559-562, September 2009.
- [6] D. F. Heidel, K. P. Rodbell, P. Oldiges et al., "Single-event-upset critical charge measurements and modeling of 65 nm silicon-on-insulator latches and memory cells," *IEEE Transactions on Nuclear Science*, vol. 53, no. 6, pp. 3512-3517, 2006.
- [7] J. A. Pellish, M. A. Xapsos, K. A. Label et al., "Heavy ion testing with iron at 1 GeV/amu," *IEEE Transactions on Nuclear Science*, vol. 57, no. 5, pp. 2948-2954, 2010.
- [8] V. Ferlet-Cavrois, J. R. Schwank, S. Liu et al., "Influence of beam conditions and energy for SEE testing," *IEEE Transactions on Nuclear Science*, vol. 59, no. 4, pp. 1149-1160, 2012.
- [9] J. R. Schwank, M. R. Shaneyfelt, V. Ferlet-Cavrois et al., "Hardness assurance testing for proton direct ionization effects," *IEEE Transactions on Nuclear Science*, vol. 59, no. 4, pp. 1197-1202, 2012.
- [10] S. R. Messenger, E. A. Burke, G. P. Summers, and R. J. Walters, "Limits to the application of NIEL for damage correlation," *IEEE Transactions on Nuclear Science*, vol. 51, no. 6, pp. 3201-3206, 2004.
- [11] G. I. Zebrev, I. O. Ishutin, R. G. Useinov, and V. S. Anashin, "Methodology of soft error rate computation in modern microelectronics," *IEEE Transactions on Nuclear Science*, vol. 57, no. 6, pp. 3725-3733, 2010.
- [12] J. Barak, "Analytical microdosimetry model for proton-induced SEU in modern devices," *IEEE Transactions on Nuclear Science*, vol. 48, no. 6, pp. 1937-1945, 2001.
- [13] F. H. Attix, *Introduction To Radiological Physics and Radiation Dosimetry*, John Wiley & Sons, Weinheim, Germany, 2004.
- [14] A. Chatterjee and H. J. Schaefer, "Microdosimetric structure of heavy ion tracks in tissue," *Radiation and Environmental Biophysics*, vol. 13, no. 3, pp. 215-227, 1976.
- [15] E. J. Kobetich and R. Katz, "Energy deposition by electron beams and  $\delta$  rays," *Physical Review*, vol. 170, no. 2, pp. 391-396, 1968.
- [16] A. Cauchy, "Mmoire sur la rectification des courbes et la quadrature des surfaces courbes," in *Oeuvres Compltes*, pp. 167-177, Gauthier, Paris, France, 1908.

- [17] P. D. Bradley, A. B. Rosenfeld, and M. Zaider, "Solid state microdosimetry," *Nuclear Instruments and Methods in Physics Research B*, vol. 184, no. 1-2, pp. 135–157, 2001.
- [18] D. A. Rajon and W. E. Bolch, "Interactions with 3D isotropic and homogeneous radiation fields: a Monte Carlo simulation algorithm," *Computer Methods and Programs in Biomedicine*, vol. 70, no. 2, pp. 167–177, 2003.
- [19] F. B. Brown and Y. Nagaya, "The MCNP5 random number generator," *Transactions of the American Nuclear Society*, vol. 87, pp. 230–232, 2002.
- [20] R. Coleman, "Random paths through rectangles and cubes," *Metallography*, vol. 6, no. 2, pp. 103–114, 1973.